Polymer Testing 150 (2025) 108927

Contents lists available at ScienceDirect

Polymer Testing

journal homepage: www.elsevier.com/locate/polytest

Stress triaxiality and failure in SFRPs: a novel workflow for failure curve determination, considering fibre orientation and specimen geometry

F.E. Fiorini [a,b,*], A. Canegrati [b], L.M. Martulli [b], P. Steck [a], A. Bernasconi [b]

[a] Thyssenkrupp Presta AG, Competence Centre Mechanics, Principality of Liechtenstein
[b] Politecnico di Milano, Mechanical Engineering Department, Via La Masa 1, 20156, Milano, Italy

ARTICLE INFO

Keywords:
Mechanical properties
Anisotropy
Failure
Stress triaxiality
Finite element analysis
Short fibre-reinforced polymers
Fracture surface analysis

ABSTRACT

This research investigates the static failure behaviour of a PA6T/6I GF50, focusing on the distribution of the stress triaxiality at critical points where failure is expected. The study explores whether a relationship exists between this stress state indicator and the strain experienced by the material, providing insights into when critical failure conditions are reached. Experimental tests, including uniaxial, biaxial, bending and shear, were conducted on various specimen types and loading orientations relative to their injection moulding direction. Finite element simulations, accounting for material's anisotropic elasto-plastic response, were run to evaluate the critical local stresses at failure locations. Digital image correlation was employed throughout the test campaign to monitor strain evolution. The evolution of the stress triaxiality during loading was computed from simulation results at both the macro (composite level) and micro-scales (matrix level). At the macro scale, it was evaluated using both isotropic (von Mises) and anisotropic (Hill 48) yield models. However, neither approach successfully identified generalized failure curves, as those correlating stress triaxiality with equivalent plastic strain, applicable across all loading scenarios and specimen geometries. To overcome this limitation, a new approach based on the calculation of the stress triaxiality and equivalent plastic strain locally at critical failure points was proposed. This allowed the identification of a failure curve that is independent of loading conditions and specimen geometry, underscoring the importance of triaxiality-based material characterization over traditional uniaxial approaches for accurately predicting failure in anisotropic short fibre-reinforced polymers.

1. Introduction

The climate crisis demands fuel-efficient vehicles, prompting automotive stakeholders to prioritize lightweight, environmentally friendly designs. This urgency underscores the need for composite materials like Short Fibre Reinforced Polymers (SFRPs), offering both design flexibility and cost-effectiveness in automotive manufacturing.

SFRPs, typically manufactured using the injection moulding process, are inherently inhomogeneous and anisotropic. The combination of their microstructural features and the mechanical behaviour of their constituents governs their macroscopic mechanical properties. The matrix is generally isotropic, while the fibres make the overall composite anisotropic. The fibres orientation significantly affects the composite's material properties [1–3] determining its level of anisotropy.

The injection moulding manufacturing process induces a locally variable fibre orientation distribution within the component and across its thickness. The microstructure was extensively studied in the literature and is commonly referred to as a skin-shell-core microstructure [1,4–7]. In the skin layer, fibres exhibit a random in-plane orientation, while the shell layer predominantly contains highly oriented fibres aligned with the flow direction. In contrast, fibres in the core layer are predominantly transverse to the flow direction.

The accurate modelling and prediction of the mechanical behaviour of SFRPs components is essential for their wide deployment across the automotive industry. Their mechanical behaviour may be determined by solving numerically Representative Volume Element (RVE), containing several instances of the fibre phase scattered in the matrix. However, this approach is generally computationally expensive, cumbersome and time-consuming [8]. The state of the art about numerical simulations of SFRP parts considers approaches in which a mean field material homogenization is implemented. The mean-field homogenization methods compute the macroscopic response of a multi-phase material analytically. An extensively used approach is the homogenization scheme conceived by Mori-Tanaka [9] based on an approximated solution of

* Corresponding author. Thyssenkrupp Presta AG, Competence Centre Mechanics, Principality of Liechtenstein.
E-mail address: francesco.fiorini@thyssenkrupp-automotive.com (F.E. Fiorini).

https://doi.org/10.1016/j.polymertesting.2025.108927
Received 31 January 2025; Received in revised form 3 June 2025; Accepted 11 July 2025
Available online 12 July 2025

Eshelby's inclusion theory [10] for multi-inclusion problem. Doghri and Tinel [11] developed a refined solution consisting of a two-step homogenization process accounting for heterogeneous fibre orientation and elasto-plastic material behaviour. A material volume is seen as an aggregate of "pseudo-grains", two-phase composites with identical and aligned fibres. The first step involves the homogenization of each individual pseudo-grain; the second one comprises the homogenization of all the pseudo-grains in the considered domain. As a result, the fibre orientation dependent homogenized mechanical properties of the composite at the macro-scale are obtained. Kammoun [12] introduced an anisotropic damage model at pseudo-grain level in the second homogenization step of the procedure.

The orientation of fibres in SFRP components is often determined through injection simulations or μCT scans of material samples. FE tools then integrate this fibre orientation data to evaluate composite properties at the element level. This allows detailed and accurate static numerical simulations at the component level to be run [13]. Subsequently, 3D strain or stress-based Tsai-Hill or Tsai-Wu brittle failure criteria [14] are applied at the pseudo-grain level to simulate the progressive failure of the composite. The results of these simulations are typically expressed in terms of failure indices, which are parameters of significant industrial interest and are useful in the design stage for identifying possible potential weak spots of the component.

Nevertheless, a significant limitation of this approach is its reduced accuracy in predicting failure following substantial plastic deformation. Consequently, there is a necessity to develop a static failure approach capable of identifying ductile failures in specimens or components. The damage accumulation and the failure mode of ductile materials are governed by stress triaxiality [15,16], a non-dimensional parameter which compare the hydrostatic and the deviatoric components of the stress tensor. Under the assumption of yielding independency on the hydrostatic stress, a yield criterion formulated on the Von Mises equivalent stress applies for isotropic ductile materials. However, for anisotropic materials like SFRPs, dual-phase steel, or rolled aluminium sheets, it loses relevance.

To address anisotropy in ductile failure, Park [17] proposed an updated definition of the stress triaxiality based on Hill's 48 [18] yield function for orthotropic materials. Rickhey and Hong [19] investigated the role of the yield model in the definition of the stress triaxiality for anisotropic materials. They applied the Von Mises, Hill 48, and Barlat 89 [20] yield models to a mild anisotropic dual-phase steel DP780 and to a high anisotropic zirconium alloy Zirlo. The authors reported a significant influence of the choice of yield model on stress triaxiality, particularly for highly anisotropic materials.

Several attempts were made to investigate the effect of stress triaxiality on the yield surface and on the failure strain of SFRPs. Particularly, Camanho et al. [21] and Vogler et al. [22] developed transversely isotropic elasto-plastic constitutive equations, considering the effect of stress triaxiality on yielding, to predict the failure onset and propagation of unidirectional plies structure. To the best of authors' knowledge, the influence of the stress triaxiality on the failure strain of SFRP was investigated only by Quagliato [23]. Through a combination of experimental data and Finite Element Analysis (FEA), a function correlating failure strain and stress triaxiality was estimated. This function was then applied as a failure criterion to predict the failure of simulated complex SFRP components.

The approach proposed by Quagliato [23] applies an isotropic yield criterion for the homogenized composite, which however still retains directional mechanical properties. Therefore, an anisotropic yield criterion might be considered especially for SFRP volume elements locally multi-axially loaded.

The appeal of stress triaxiality to the industry stems from its potential as a ductile damage parameter capable of predicting failure under high plastic strain conditions. The "*FKM (Forschungskuratorium Maschinenbau) guideline for nonlinear strength assessment of mechanical components*" [24] has garnered considerable attention in the industry for its applicability in industrial design. This guideline provides a comprehensive procedure that facilitates the interpretation of component level FEA results. The equivalent plastic strain and the stress triaxiality quantities play pivotal roles in strength assessment and estimation of safety operational margins for metallic components. The evolution of the stress triaxiality with the equivalent plastic strain, evaluated in critical areas of the component, is plotted in the so-called Triaxiality Failure Diagram (TFD) and compared to the material limit curves.

While effective for metallic materials, it lacks specific guidance for polymeric materials like SFRPs. This gap requires continuous health monitoring using complex and costly software-based methods. Our research aims to bridge this gap by providing tailored guidance for static strength assessment of SFRPs, enhancing efficiency and accuracy in structural design processes, particularly in the automotive industry.

Predicting ductile failure is crucial in various industries, particularly in automotive, where stringent requirements demand accurate simulations of plastic behaviour in components. In many cases, the occurrence of crack initiation during specific load scenarios is not permissible. Therefore, the development and implementation of reliable failure prediction methods become essential. Utilizing parameters such as triaxiality and plastic strain offers a promising approach in this regard. By leveraging these metrics, engineers can better understand the conditions under which cracks are likely to initiate, thus enabling proactive measures to prevent failures and ensure the durability and safety of automotive components.

Within this paper, the relationship between stress triaxiality and failure strain of SFRP is investigated, considering the role of fibre orientation and loading conditions. First, an extensive experimental database on different specimens and loading conditions was generated. Then, an advanced numerical workflow, which integrates the microstructural information, material modelling, and structural analysis of tested specimens, was implemented. This facilitated the precise prediction of mechanical behaviour and allowed for numerical evaluation of stress triaxiality and equivalent plastic strain at both macro (composite) and micro (matrix) scales. The novelty of this study lies in its ability to correlate local stress triaxiality with failure behaviour, overcoming the limitations of conventional uniaxial approaches. A new approach is thus proposed, which combines a new experimental campaign with simulations, to enable the determination of failure curves that are independent of specimen geometry and loading conditions, providing a robust framework for the accurate characterisation of anisotropic short fibre-reinforced polymers.

2. Material and methods

2.1. Material and specimens manufacturing

The material under investigation is a PA6T/6I, reinforced with 50 % in weight short glass fibres, commercially known as Ultramid® Advanced T1000HG10 and supplied by BASF SE [25]. To explore the local stress distribution induced by the fibre orientation for a given external load, variously shaped and oriented specimens were obtained from injection-moulded plates (150 mm × 150 mm) with a thickness (t) of 3 mm. The specimen milling area (130 mm × 130 mm) is illustrated in Fig. 1(a). The design of the specimens' geometries and test configuration was tailored to induce distinct nominal stress triaxiality in an equivalent homogenous isotropic material. Fig. 1(b) shows the specimens' shape and dimensions and introduces the specimens' nomenclature. Except for the disk specimens, one specimen per plate was machined at angles of 0°, 45°, and 90° with respect to the main flow direction. The shear, dog bone, and disk specimens were selected to investigate deviations in stress triaxiality from nominal values due to the heterogeneous anisotropic nature of the SFRPs. Dog bone specimens with double notches and holes were chosen to further analyse the effect of stress concentrations induced by geometrical discontinuities on SFRPs' stress triaxiality. Additionally, a specimen geometry known for the Nakajima test,

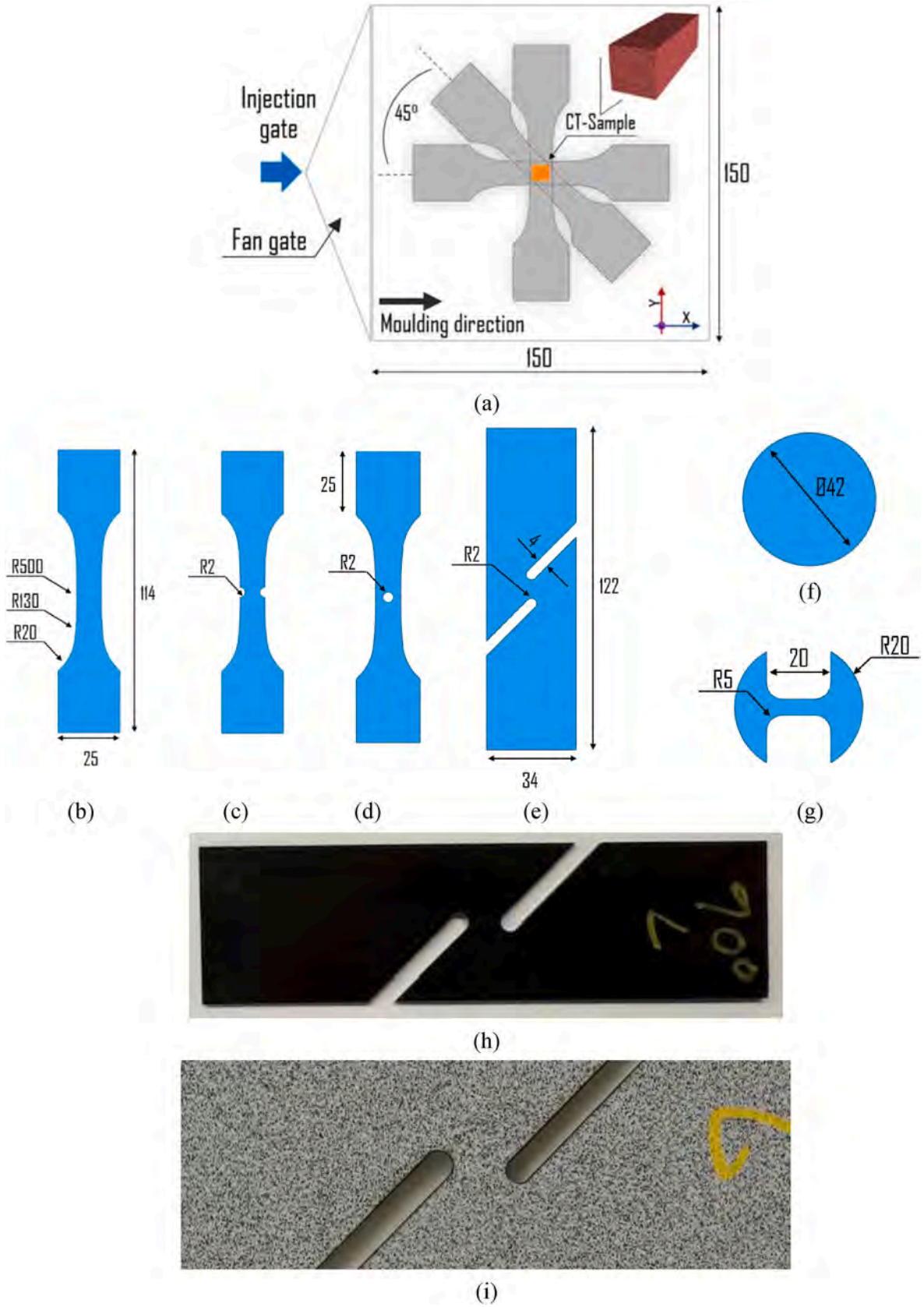

Fig. 1. (a) Plate dimensions, specimen cutting areas, and CT-sample position. Dimensions for (b) dog bone, (c) dog bone with a double notch, (d) with a hole (e) shear, (f) disk and (g) Nakajima specimen. (h) Shear specimen after cutting; (i) shear specimen after speckle pattern application in measurement area, prior to testing.

according to EN ISO 12004–2:2021 [26], was designed to enable bending tests on the same device used for testing disk specimens under biaxial loads. Further details about the purpose-built device are provided in Section 2.2.2.

2.2. Experimental methods

2.2.1. Microstructural characterisation: μCT and SEM analysis

To characterise the microstructure and failure behaviour of the material, two complementary techniques were employed: μCT scanning and fracture surface analysis via Scanning Electron Microscopy (SEM). While μCT scanning provided a non-destructive three-dimensional visualisation of the fibre orientation and distribution within the material, SEM analysis enabled a detailed inspection of fracture surfaces to assess failure mechanisms at the microscale.

2.2.1.1. μCT scanning.

μCT scans were conducted at maXerial AG using a Phoenix V|tome|x M300 computer tomography system from Waygate Technologies [27]. The tube voltage and current were set at 150 kV and 50 μA, respectively, with a 0.5 mm aluminium filter positioned directly before the X-ray tube. Three samples were projected onto a Dynamic 41|200p + detector with a resolution of 2048 x 2048 pixels and a pixel pitch of 200 μm. The volume was reconstructed from 2300 2D projections, each with an exposure time of 100 ms. The resulting volume had a voxel resolution of 8 μm. Rendering, visualization, and fibre orientation determination were performed using VG Studio Max. 3.2 software from Volume Graphics [28].

Fig. 1(a) illustrates the μCT scanning sample (0.83 mm × 0.83 mm x 3 mm) extracted from the plate. Notably, the analysed microstructure is representative of all specimens since they were extracted from the same position on the plate.

2.2.1.2. Fracture surface analysis. The fracture surfaces of the specimens were analysed using SEM to identify distinct regions of matrix failure, such as micro-ductile or micro-brittle fracture characteristics. Given the high fibre content of the material, the macroscopic stress-strain behaviour was expected to be predominantly linear, with limited plasticity due to the material's high stiffness and reinforcement. At the microscale, the investigation focused on detecting evidence of plastic deformation within the matrix phase, particularly in critical regions or areas of stress concentration.

The surface microstructure analysis was performed using a TESCAN Vega-III high-resolution SEM [29], equipped with an energy-dispersive spectrometer. The instrument was operated in high vacuum mode to ensure optimal imaging conditions. The specimen surfaces were coated with a thin layer of gold to enhance electrical conductivity and improve imaging contrast and resolution before examination.

2.2.2. Mechanical testing methods

To maintain a moisture content below 0.1 %wt., all the specimens were individually sealed immediately after manufacturing, then stored in waterproof bags until testing.

Displacement-controlled uniaxial quasi-static tests were carried out using an MTS RF/100 testing machine equipped with a 100 kN load cell. The displacement rate was set to 1 mm/min. Strain measurements were obtained using a 3D optical measurement system, GOM ARAMIS [30]. The two 12 megapixel cameras of the 3D system were positioned at a measuring distance d of 266 mm, and the resulting angle α between the specimen and the two cameras was set to 25°. The distance between the two cameras D was set to 79 mm. The cameras were positioned at a height that framed the central region of the specimens' gauge length within the measuring volume of the system, which was 35 mm × 46 mm x 10 mm. Two Schneider lenses with a 50 mm focal length were used. This setup was employed to measure the frontal major and minor strains during the testing of the dog bone, the dog bone with a hole, the dog bone with a double notch, and the shear specimens.

Three of the six tested dog bone specimens with a hole and a double notch at all orientations were tested with 90° rotated grips to enable a sideways view of the specimen. This configuration allowed for strain measurements on the curved side surfaces of the notch and the hole.

To facilitate the measurement of local strains during testing using Digital Image Correlation (DIC), an innovative test device, shown in Fig. 2, was designed and utilised for both the Nakajima and disc specimens. Owing to the proximity of the cameras to the specimens, the device provides precise strain measurements, which are essential for subsequent numerical analysis. Additionally, the device enables the application of a biaxial loading condition, allowing for more comprehensive testing. Thus, the proposed device overcomes the limitations of uniaxial tests and supports detailed characterisation under various loading conditions.

The two cameras, used during the strain measurement, were positioned at a horizontal measuring distance d_x of 188 mm. The angle φ that the specimen makes with the two cameras in the side view of the layout was set to approximately 45°. The angle α that the specimen makes with the two cameras in the top view of the layout was set to 25°. The camera-specimen configuration, shown in Fig. 3, allows the central part of the disk and Nakajima specimens to be framed within the measuring volume of the Aramis system, which was 35 mm × 46 mm x 10 mm.

Displacement-controlled uniaxial compressive tests were run on a MTS Criterion® C42 electromechanical testing machine, equipped with a 2 kN load cell, at a crosshead displacement rate of 1 mm/min.

The test device is anchored from the *basement* to the testing machine fixed compressive plate. The lower screw hosts the specimen within a dedicated housing. The fastening between the upper and lower screws (constituting *subsystem 1*) occurs by a threaded mechanism. This also provides the clamping of specimen by its edge within the *subsystem 1*. The moving compressive plate of the testing machine pushes against the upper screw of *subsystem 1,* which in turn slides on the *slider* (*subsystem 2*). Depending on the tested specimen, *tool a* or *tool b* were fixed to the slider when testing the disk or the Nakajima specimens, respectively. After fixing the *basement*, the uniaxial testing machine's moving grip applies compression force to the *upper screw's* surface, initiating a downward sliding movement of *subsystem 1* on the *slider*. The force and displacement data, obtained from the machine software, represent the

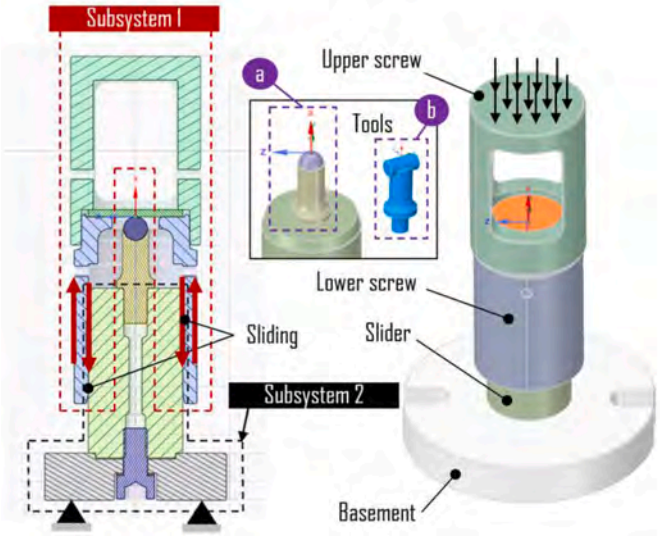

Fig. 2. Auxiliary test device designed for the characterization of the disk and Nakajima specimens.

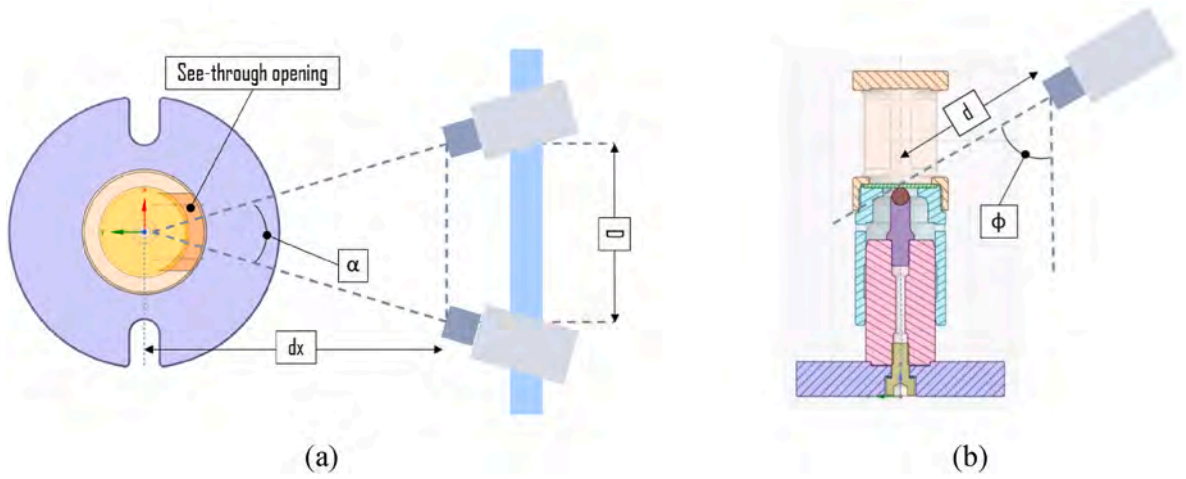

Fig. 3. Schematically (a) top and (b) side view of the test set-up with relevant dimensions.

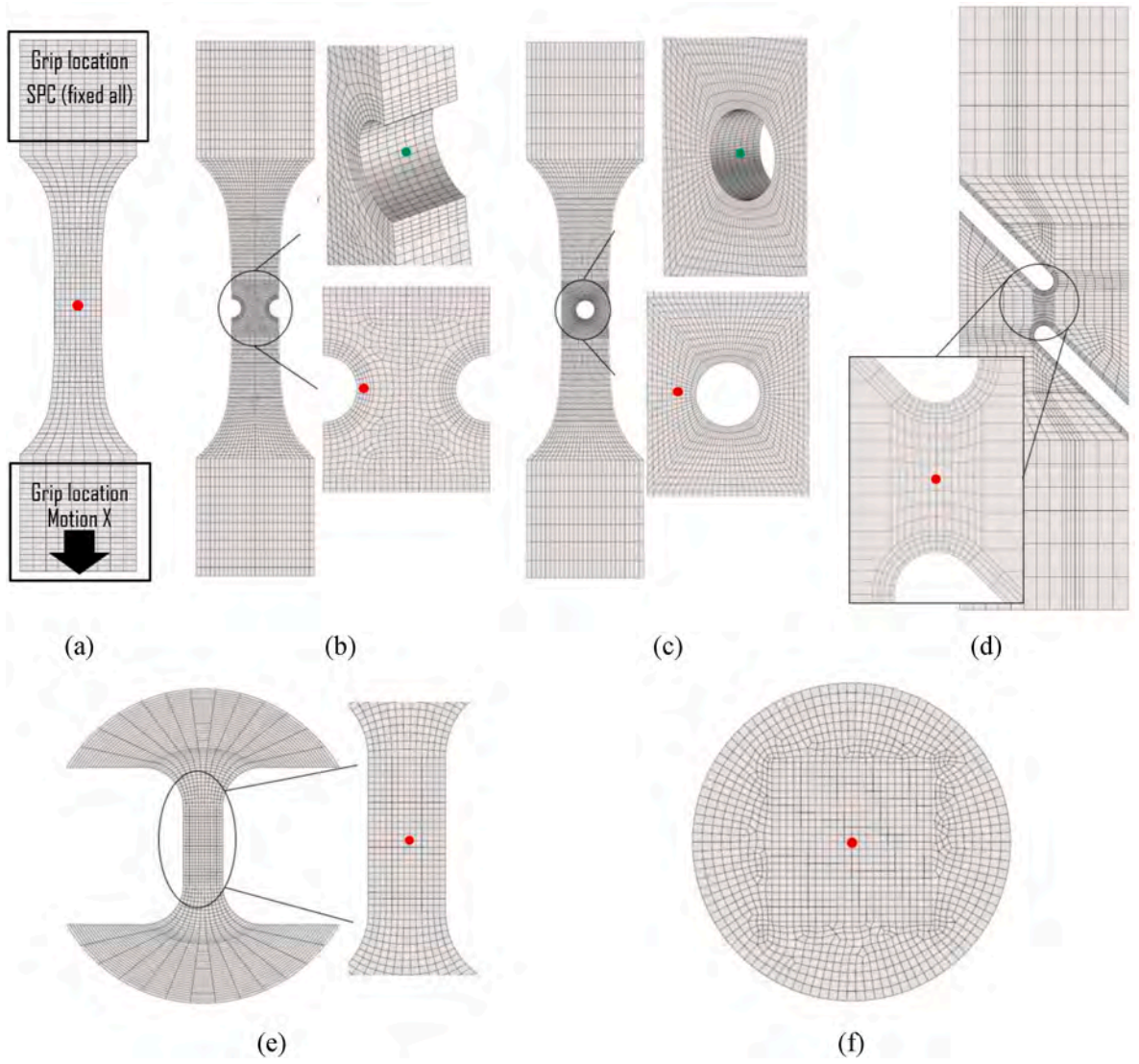

Fig. 4. (a–f) FE discretization for the simulated specimens. The red and green dots represent the frontal and side evaluation points of the relevant mechanical quantities used by the DIC and FEA. FE boundary conditions for the (a) dog bone, (b) dog bone with a double notch, (c) with a hole and (d) shear specimen.

stiffness curve of the tested specimen. The windows on the *upper screw* allow the local strain measurement to be carried out using the DIC during testing. This setup enables biaxial or bending testing on a uniaxial tensile machine. Six specimens per orientations and specimen type were tested. A random speckle pattern was applied to the specimens for this measurement. Given the specimens' gloss black finish, they were initially coated with matt black paint. Once the paint dried, white fine speckle patterns were sprayed onto them. Fig. 1(h) shows the specimen before speckling, and Fig. 1(i) after the speckle pattern was applied.

2.3. Numerical methods

In this research, the commercial software *Ansys® Workbench 2022 R2* [31] was used to perform the structural simulations. The FE software enables the assessment of the overall specimen response, encompassing force and displacement, as well as the characterization of local strain and stress fields within the specimen, which vary based on its microstructure and orientation.

2.3.1. Description of the finite element model

The FE analyses were conducted using the implicit FE-Solver *Ansys® Mechanical 2022 R2*. The meshes, consisting of volume hexahedral elements (Solid186 [32]), selected for all specimens are illustrated in Fig. 4. An element edge length of 0.375 mm was employed, and eight elements across the thickness were utilized. To support the mesh selection, we performed a mesh sensitivity analysis on all specimen types, with detailed results provided in the supplementary materials (Fig. S1–S2). For the dog bone specimen, where a uniform stress distribution is expected due to remote uniaxial loading and the absence of geometric discontinuities, no significant variation in triaxiality or other mechanical quantities was observed within the evaluation region. This is illustrated in Fig. S1: the triaxiality distribution for the coarser mesh used in the main analysis is shown in Fig. S1(a), with a zoomed-in view in Fig. S1(b) confirming the uniformity across the region.

A comparison with a finer mesh (Fig. S1(c)) shows negligible differences, confirming that the selected mesh is sufficiently refined.

A similar analysis was conducted for the Nakajima and disk specimens, which feature more complex stress states due to bending and localised loading. As shown in Fig. S2(a–c), only minor local differences in triaxiality were observed between coarse and refined meshes, with no impact on the conclusions. These results confirm the robustness of the selected mesh across all configurations.

A finer local mesh element size of 0.18 mm was chosen for the shear specimen and for the dog bone specimen with a hole and with a double notch to enhance mesh quality and ensure a more accurate representation of geometric features.

Fig. 5 illustrates the boundary conditions for the disk and Nakajima specimens. The upper and lower screw, as well as the tool, were modelled as rigid bodies. For the contact interfaces between the specimen and the upper and lower screw, and tool, a frictional contact with a coefficient of friction set to 0.1 was used [33].

To simulate the anisotropic behaviour of the specimen, coupled FE simulations where performed. The coupled simulation allows the transfer of the fibre orientation dependent local material properties into the mechanical FE model.

Two approaches were considered to perform the coupled simulation. In the first approach, the investigation of the macro-scale behaviour of the specimen was carried out by using the Ansys® Material Designer (MD) [34] software as coupler. The use of MD simplifies and integrate the whole workflow within a single software suite [31]. However, MD limits the analysis to the macro-scale, as it computes only homogenised mechanical quantities at the composite level. This prevents the evaluation of phase-specific responses, such as matrix stress or strain, even in an averaged sense. While the matrix and fibre phases are individually defined as linear elastic at the micro-scale, plasticity is introduced at the macro-scale through the composite's homogenised response. Consequently, nonlinearity in the matrix phase itself cannot be explicitly captured.

In the second approach, instead, the micro-scale behaviour of the specimen was analysed by using the Digimat [35] software package. Despite the drawback of splitting the set-up of the simulation on different software, Digimat enables the micro-scale computation of volume-averaged mechanical quantities, i.e. at constituents' level. Further, it allows the definition of an elasto-plastic constitutive model for the matrix material. It worked with a J2-plasticity criterion coupled with an isotropic hardening model, described by an exponential and linear law [35].

Both approaches require the generation of a homogenized material model for the composite, which is based on identical inputs: the constitutive models of the composites' individual constituents, a suitable mean-field homogenization method and the parameters which describe the material microstructure.

The second order, two-steps Mori-Tanaka [9] scheme was applied for the homogenization of the elastic material properties, in both the approaches. However, in the first approach (MD), an orientation dependent Hill yield criterion [18], combined with a multilinear isotropic hardening model, was used to describe the plastic response of the homogenized material [35]. The multilinear isotropic hardening model uses a piecewise linear approximation to define how the material's yield surface evolves during plastic deformation. Conversely, in the second approach (Digimat software), the orientation dependent plastic response of the composite is defined through an extension of the Mori-Tanaka [9],

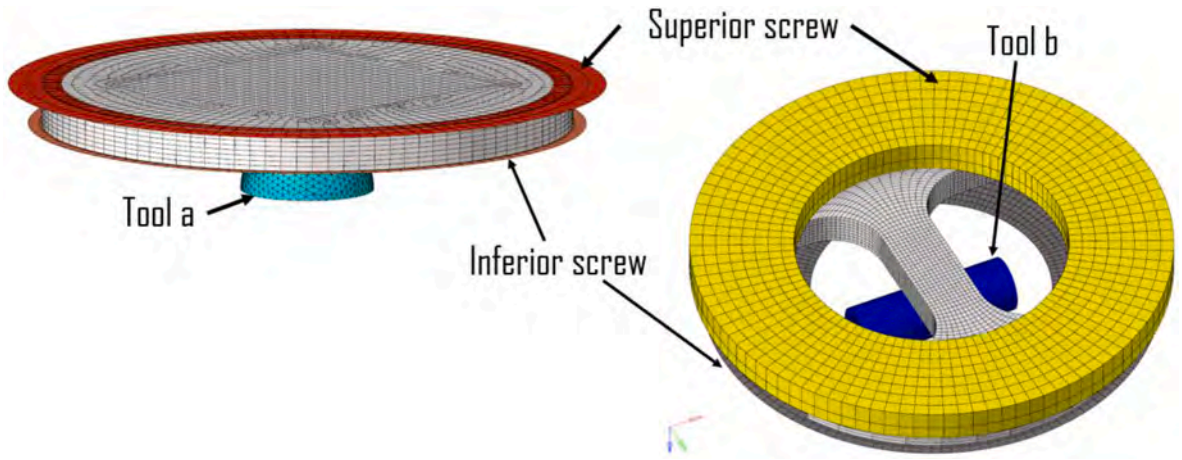

Fig. 5. FE models using Ansys® Mechanical 2022 R2 for the disk and Nakajima specimens.

Table 1
Summary of material modelling approaches used in ANSYS MD and Digimat.

Modelling	Ansys Material Designer (MD)	Digimat MF
Matrix model	Linear elastic	Elasto-plastic (J2 plasticity + isotropic hardening)
Matrix input parameter	Elastic modulus (E), Poisson's ratio (ν) Reverse engineering from 0° and 90° tensile tests	E, ν, yield stress, plastic hardening curve (exponential linear law)
Fibre model	Linear elastic, isotropic	Linear elastic, isotropic
Fibre input parameters	E, ν (standard values for short glass fibres)	
Homogenisation scheme	Mori-Tanaka	Mori-Tanaka
Modelling approach	Single-software workflow with simplified material description	Coupled workflow (Digimat for multiscale material; ANSYS for structural FE)
	Only composite-level response available	Phase-level response (matrix and fibre stresses/strains) accessible
	Matrix modelled as linear elastic; non-linearity introduced at composite level (fitted using tensile tests)	Matrix modelled with plasticity

which generalizes the strain concentration tensors and constitutive relations to account for nonlinear inelastic behaviour. This method is based on the concept of the incremental formulation of the non-linear range of the stress-strain curve, which relates stress and strain rates with anisotropic tangent operators, for each phase. However, satisfactory homogenisation outcomes may be obtained by properly using an isotropic part of the tangent operator, as extensively studied in Ref. [36]. The modified spectral decomposition method [37,38], implemented in Digimat [35], was specifically adopted for the isotropisation.

In both the approaches the same microstructural information, evaluated by analysis of the μCT scans, (see Section 2.2.1), and the same isotropic linear elastic formulation of the fibre behaviour, whose parameters were set consistently with those of glass fibres standardly employed in SFRPs, were used. The parameters of the matrix constitutive models were instead calibrated through reverse engineering from experimental stress-strain curves of dog-bone specimens, milled-out from injected plates (see Fig. 1(a)) longitudinally and transversally to the main flow direction, i.e. with orientations of 0° and 90°, respectively. The calibrated parameters of the material models cannot be disclosed due to confidentiality.

For a comprehensive description of the material modelling techniques implemented in the commercially available software, including rigorous mathematical formulations, the required parameters for calibration, and details on the reverse engineering workflow, the reader is referred to the software documentation provided in Refs. [34,35].

A summary of the modelling approaches and material definitions used in ANSYS MD and Digimat is provided in Table 1, highlighting the key differences in constitutive models, input parameters, and homogenisation strategies.

2.3.2. Data post-processing

The relevant results of the simulations were the stress $\bar{\bar{\sigma}}$ and the plastic strain $\bar{\bar{\varepsilon}}^{pl}$ symmetric tensors, from which the stress triaxiality and the equivalent plastic strain are calculated. These parameters could be used, respectively, as indicators of the stress and strain state of the material, to build the Triaxiality Failure Diagram (TFD). All the values used for stress triaxiality and equivalent plastic strain calculations were extracted from structural simulations in correspondence to the experimental failure point.

In the post-processing of the simulation outcomes, two reference frames were used:

- **Cartesian:** this is the global reference frame, defined by the three standard mutually orthogonal axes (x, y, z). The tensorial quantities which refer to the cartesian reference frame will be denoted by subscripts $\boldsymbol{i}.\boldsymbol{j}$.
- **Microstructural:** this is the local reference frame, defined by the principal axes of the material anisotropy (1,2,3). These are defined as the intersections of the three planes of symmetry. Note that, in SFRPs, the principal axes of anisotropy coincide with the principal directions of the local fibre orientation tensor. The tensorial quantities which refer to the microstructural reference frame will be denoted by subscript $\boldsymbol{k},\boldsymbol{l}$.

Stress triaxiality: In the three-dimensional stress state, described by the tensor $\bar{\bar{\sigma}}$, the stress triaxiality η is defined as the ratio of the hydrostatic stress, σ_h, to an equivalent stress σ_{eq}. The hydrostatic stress is, by definition, the average of the normal stresses, σ_{ii}, of $\bar{\bar{\sigma}}$. Thus, it is one third of the first invariant of the stress tensor I_1, i.e. the trace of $\bar{\bar{\sigma}}$. It is worth mentioning that σ_h does not change with the orientation of the reference frame considered for the stress analysis. The expression of the stress triaxiality, η, is:

$$\eta = \frac{\sigma_h}{\sigma_{eq}} = \frac{I_1}{3\sigma_{eq}} = \frac{\mathrm{tr}(\bar{\bar{\sigma}})}{3\sigma_{eq}} = \frac{1}{3}\left(\frac{\sigma_{xx}+\sigma_{yy}+\sigma_{zz}}{\sigma_{eq}}\right) \tag{1}$$

Where σ_{xx}, σ_{yy} and σ_{zz} are the normal stresses in the directions of the reference frame's axis and $\mathrm{tr}(\bar{\bar{\sigma}})$ is their sum. As previously mentioned, the stress triaxiality was computed both at the composite level and the matrix phase level.

2.3.2.1. Stress triaxiality at macro scale (composite level). On the composite level, two plastic potential functions and yield criteria were employed to compute the equivalent stress σ_{eq}:

(I) The **von Mises** yield criterion assumes that an isotropic material yields when its stress state dependent plastic potential, $\boldsymbol{f}(\boldsymbol{\sigma_{ij}})$, equals its uniaxial tensile yield stress squared, $\boldsymbol{\sigma_y^2}$:

$$f(\sigma_{ij}) = \frac{1}{2}\left[(\sigma_{xx}-\sigma_{yy})^2+(\sigma_{yy}-\sigma_{zz})^2+(\sigma_{zz}-\sigma_{xx})^2\right]+3\left[\sigma_{yz}^2+\sigma_{zx}^2+\sigma_{xy}^2\right]=\sigma_y^2 \tag{2}$$

leading to express the equivalent von Mises stress for isotropic materials, $\sigma_{eq}^{von\ Mises}$, as:

$$\sigma_{eq}^{von\,Mises} = \sqrt{\frac{1}{2}\left[(\sigma_{xx}-\sigma_{yy})^2+(\sigma_{yy}-\sigma_{zz})^2+(\sigma_{zz}-\sigma_{xx})^2\right]+3\left[\sigma_{yz}^2+\sigma_{zx}^2+\sigma_{xy}^2\right]} \tag{3}$$

(II) The **Hill 48** yield criterion assumes that an anisotropic material yields when its stress state dependent plastic potential, expressed in terms of its orthogonal principal axes of anisotropy $\boldsymbol{f}(\boldsymbol{\sigma_{kl}})$, equals a reference yield stress squared, $\boldsymbol{\sigma_{y,0}^2}$:

$$f(\sigma_{kl}) = F(\sigma_{22}-\sigma_{33})^2+G(\sigma_{33}-\sigma_{11})^2+H(\sigma_{11}-\sigma_{22})^2+2L\sigma_{23}^2+2M\sigma_{13}^2 + 2N\sigma_{12}^2=\sigma_{y,0}^2 \tag{4}$$

An equivalent Hill stress for anisotropic material, σ_{eq}^{Hill}, could be

therefore defined as [34]:

$$\sigma_{eq}^{Hill} = = \sqrt{F(\sigma_{22}-\sigma_{33})^2 + G(\sigma_{33}-\sigma_{11})^2 + H(\sigma_{11}-\sigma_{22})^2 + 2L\sigma_{23}^2 + 2M\sigma_{13}^2 + 2N\sigma_{12}^2} \quad (5)$$

the coefficients in the Hill's equivalent stress, σ_{eq}^{Hill}, are defined as:

$$F = \frac{1}{2}\left(\frac{1}{R_{22}^2} + \frac{1}{R_{33}^2} - \frac{1}{R_{11}^2}\right), G = \frac{1}{2}\left(\frac{1}{R_{33}^2} + \frac{1}{R_{11}^2} - \frac{1}{R_{22}^2}\right),$$
$$H = \frac{1}{2}\left(\frac{1}{R_{11}^2} + \frac{1}{R_{22}^2} - \frac{1}{R_{33}^2}\right), L = \frac{3}{2}\left(\frac{1}{R_{23}^2}\right), M = \frac{3}{2}\left(\frac{1}{R_{13}^2}\right), N = \frac{3}{2}\left(\frac{1}{R_{12}^2}\right) \quad (6)$$

with:

$$R_{kk} = \frac{\sigma_{y,kk}}{\sigma_{y,0}}, k = 1,2,3 \; R_{kl} = \sqrt{3}\,\frac{\sigma_{y,kl}}{\sigma_{y,0}}, l = 1,2,3 \text{ and } l \neq k \quad (7)$$

The R_{kk} and R_{kl} values are called yield ratios or scaling factors because they scale the reference yield stress, $\sigma_{y,0}$, from an arbitrarily defined reference curve (multilinear isotropic hardening curve), valid for a particular direction, to the yield stress in a different directions, $\sigma_{y,kk}$ and $\sigma_{y,kl}$. It is worth noting that the current definition of the stress triaxiality implies a self-dependency on the choice of the reference stress. To restore its independency on the reference stress, its definition is updated by:

- Transforming the normal stress components of the hydrostatic stress from the cartesian, $\boldsymbol{\sigma_{ii}}$, to the microstructural, $\boldsymbol{\sigma_{kk}}$, reference frame,
- Normalizing each stress component of the hydrostatic stress, $\boldsymbol{\sigma_{kk}}$, by the corresponding yield ratio, $\boldsymbol{R_{kk}}$.

The equivalent definition of stress triaxiality for the anisotropic material takes the form:

$$\eta = \frac{1}{3}\left(\frac{\frac{\sigma_{11}}{R_{11}} + \frac{\sigma_{22}}{R_{22}} + \frac{\sigma_{33}}{R_{33}}}{\sigma_{eq}^{Hill}}\right) \quad (8)$$

The R-values used in the Hill yield criterion were computed using ANSYS Material Designer, which applies mean-field homogenization based on the fibre volume fraction and orientation tensors. These yield ratios reflect the directional dependence of the composite yield behaviour and are derived from the effective anisotropic properties of the injection-moulded material. No direct RVE-based simulations were used.

2.3.2.2. Stress triaxiality at micro-scale (matrix level). At the matrix phase level, the von Mises equivalent stress yield criterion, presented in Eq. (3), was applied. The matrix stresses were computed using Digimat.

These matrix stresses were calculated using the MICRO solution method available in Digimat-RP, which is based on mean-field homogenization techniques. This approach computes phase-averaged matrix stresses dynamically during the simulation, based on local fibre orientation tensors and nonlinear material behaviour. Although it does not capture local stress concentrations as direct FEM (RVE) methods would, it enables an efficient and representative estimation of matrix-level triaxiality.

Fig. 6 depicts the range of nominal triaxiality values of a material element, starting from a biaxial compression stress state ($\eta = -0.66$) to a biaxial tensile stress state ($\eta = +0.66$). Triaxiality values of $\pm 1/\sqrt{3}$ are associated to plane strain condition under uniaxial stress, while values of $\pm 1/3$ to uniaxial stress state. The nominal stress triaxiality equals 0 for ideal shear stress state.

Equivalent plastic strain: Under the assumption that yielding depends only on the deviatoric stress tensor and that the material is incompressible at yield, the equivalent plastic strain, ε_{eq}^{pl}, a scalar measure of the plastic strain tensor, is defined through a time integration of the equivalent plastic strain rate, $\dot{\varepsilon}_{eq}^{pl}$, as:

$$\varepsilon_{eq}^{pl} = \int_{t=0}^{t} \dot{\varepsilon}_{eq}^{pl} dt \quad (9)$$

It is worth nothing that $\varepsilon_{ij}^{pl} = 0$ at $t = 0$, i.e. the onset of plasticity. The equivalent plastic strain rate is defined through an incremental plastic work balance. The incremental work which causes plastic deformation is given by the product between the stress vector, $\overline{\boldsymbol{\sigma}}$, and the plastic strain rate vector, $\dot{\overline{\boldsymbol{\varepsilon}}}^{pl}$. This is assumed to match the product between the equivalent stress, σ_{eq}, and the equivalent plastic strain rate $\dot{\varepsilon}_{eq}^{pl}$, independently on the symmetry properties of the material. The incremental plastic work balance reads:

$$\overline{\boldsymbol{\sigma}} \cdot \dot{\overline{\boldsymbol{\varepsilon}}}^{pl} = \sigma_{eq}\dot{\varepsilon}_{eq}^{pl} \quad (10)$$

Where $\overline{\boldsymbol{\sigma}}$ and $\dot{\overline{\boldsymbol{\varepsilon}}}^{pl}$ are vectors collecting the independent components of $\overline{\overline{\boldsymbol{\sigma}}}$ and $\dot{\overline{\overline{\boldsymbol{\varepsilon}}}}^{pl}$, respectively defined in the cartesian reference frame as:

$$\overline{\boldsymbol{\sigma}} = \{\sigma_{xx}\ \sigma_{yy}\ \sigma_{zz}\ \sigma_{yz}\ \sigma_{zx}\ \sigma_{xy}\}\ \dot{\overline{\boldsymbol{\varepsilon}}}^{pl} = \left\{\dot{\varepsilon}_{xx}^{pl}\ \dot{\varepsilon}_{yy}^{pl}\ \dot{\varepsilon}_{zz}^{pl}\ \dot{\varepsilon}_{yz}^{pl}\ \dot{\varepsilon}_{zx}^{pl}\ \dot{\varepsilon}_{xy}^{pl}\right\} \quad (11)$$

After some mathematical manipulations and considering the associated plastic flow rule:

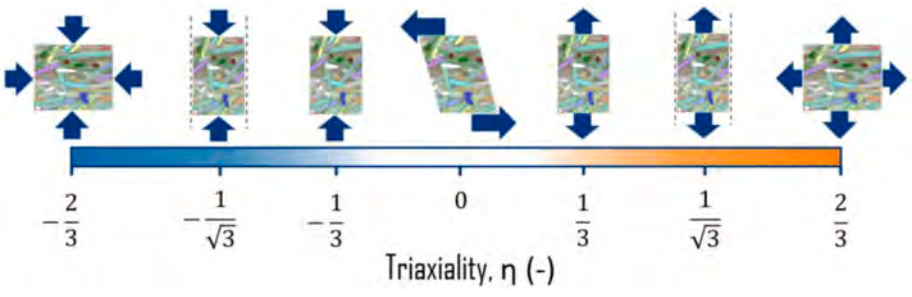

Fig. 6. Triaxiality in a bidimensional case.

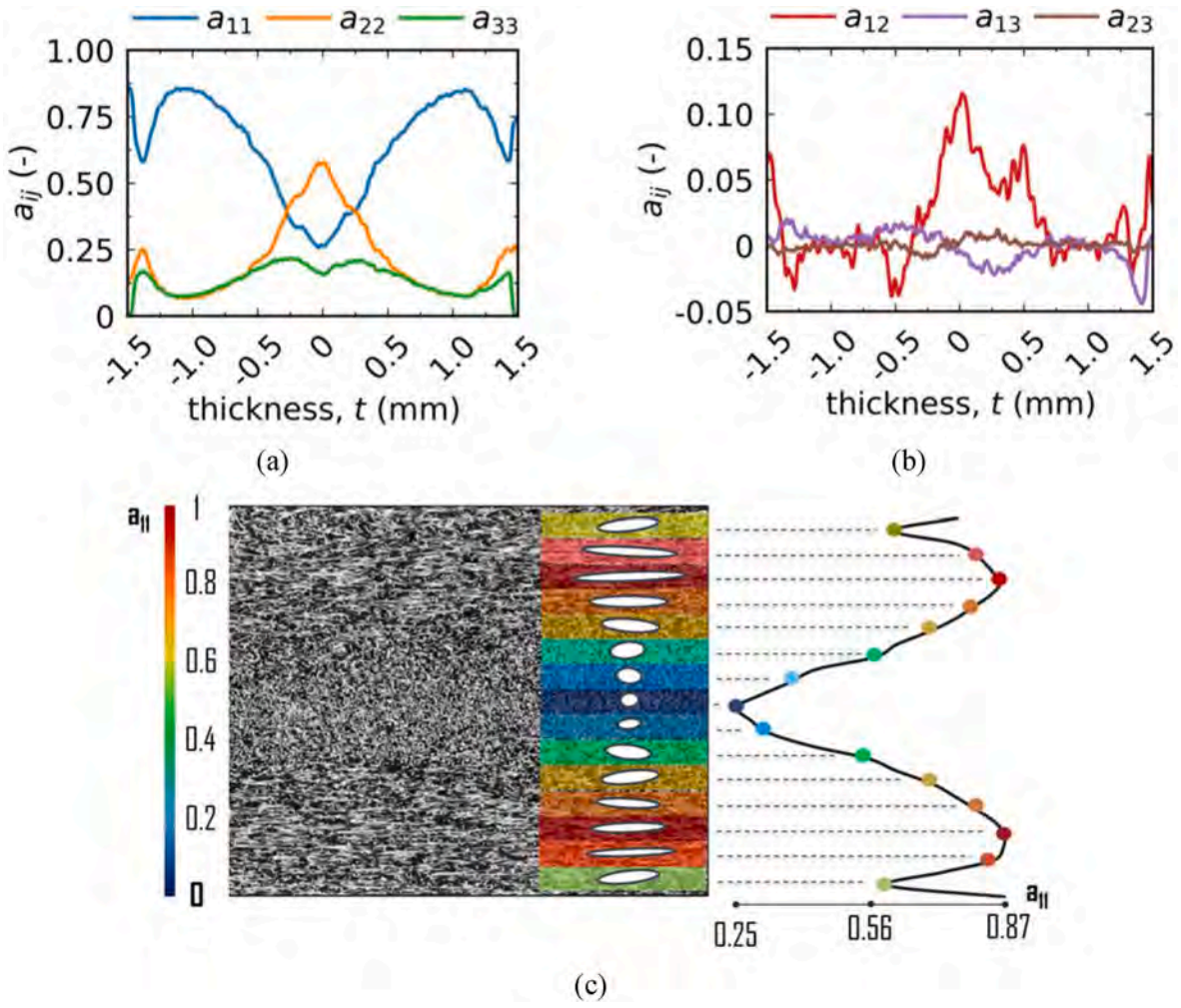

Fig. 7. Orientation tensor distribution for the (a) diagonal and for the (b) off-diagonal components. (c) Representative μCT cross-section image at the centre of the injection-moulded plate, illustrating local fibre orientations across the specimen thickness. the centre of the injection-moulded plate, illustrating local fibre orientations across the specimen thickness. The region corresponds to the same location used for orientation tensor extraction in Fig. 7a and b.

$$\dot{\bar{\boldsymbol{\varepsilon}}}^{pl} = \dot{\lambda}\frac{d\bar{f}(\bar{\boldsymbol{\sigma}})}{d\bar{\boldsymbol{\sigma}}} \tag{12}$$

The equivalent plastic strain rate for an isotropic material, derived from substituting the von Mises's plastic potential (Eq. (2)) into Eq. (12), can be expressed as:

$$\dot{\varepsilon}^{pl}_{eq,von\ Mises} = \sqrt{\frac{2}{3}\dot{\bar{\varepsilon}}^{pl}_{ij}\dot{\bar{\varepsilon}}^{pl}_{ij}} = \sqrt{\frac{2}{3}\left[\left(\dot{\bar{\varepsilon}}^{pl}_{xx}\right)^2+\left(\dot{\bar{\varepsilon}}^{pl}_{yy}\right)^2+\left(\dot{\bar{\varepsilon}}^{pl}_{zz}\right)^2\right]+\frac{4}{3}\left[\left(\dot{\bar{\varepsilon}}^{pl}_{yz}\right)^2+\left(\dot{\bar{\varepsilon}}^{pl}_{zx}\right)^2+\left(\dot{\bar{\varepsilon}}^{pl}_{xy}\right)^2\right]} \tag{13}$$

Similarly, the equivalent plastic strain rate for an anisotropic material, stemming from substituting the Hill's plastic potential (Eq. (4)) in Eq. (12), can be expressed as:

$$\dot{\varepsilon}^{pl}_{eq,Hill} = \sqrt{\frac{F\left(\dot{\bar{\varepsilon}}^{pl}_{11}\right)^2+G\left(\dot{\bar{\varepsilon}}^{pl}_{22}\right)^2+H\left(\dot{\bar{\varepsilon}}^{pl}_{33}\right)^2}{FG+FH+GH}+\frac{2\left(\dot{\bar{\varepsilon}}^{pl}_{23}\right)^2}{L}+\frac{2\left(\dot{\bar{\varepsilon}}^{pl}_{31}\right)^2}{M}+\frac{2\left(\dot{\bar{\varepsilon}}^{pl}_{12}\right)^2}{N}} \tag{14}$$

For a rigorous and detailed mathematical derivation of Eq. (13) and Eq. (14) the reader is referred to Ref. [34]. It is worth noting that time independent material properties were considered for the structural simulations, consequently their outcomes feature the same time independency. Therefore, for the current analysis, the plastic strain rate vector $\dot{\bar{\boldsymbol{\varepsilon}}}^{pl}$ loses its time dependency and becomes equivalent to the plastic strain increment vector $\Delta\bar{\boldsymbol{\varepsilon}}^{pl}$, defined as:

$$\dot{\bar{\boldsymbol{\varepsilon}}}^{pl} \equiv \Delta\bar{\boldsymbol{\varepsilon}}^{pl} = \left\{\Delta\bar{\varepsilon}^{pl}_{xx}\ \ \Delta\bar{\varepsilon}^{pl}_{yy}\ \ \Delta\bar{\varepsilon}^{pl}_{zz}\ \ \Delta\bar{\varepsilon}^{pl}_{yz}\ \ \Delta\bar{\varepsilon}^{pl}_{zx}\ \ \Delta\bar{\varepsilon}^{pl}_{xy}\right\} \tag{15}$$

Where the plastic strain increment of the plastic strain component ε^{pl}_{ij} is defined as its difference over consecutive simulation steps. It naturally follows that the equivalent plastic strain rate, either defined from Von Mises or from Hill plastic potential, is equivalently defined as equivalent plastic strain increment, $\Delta\varepsilon^{pl}_{eq}$, which reads:

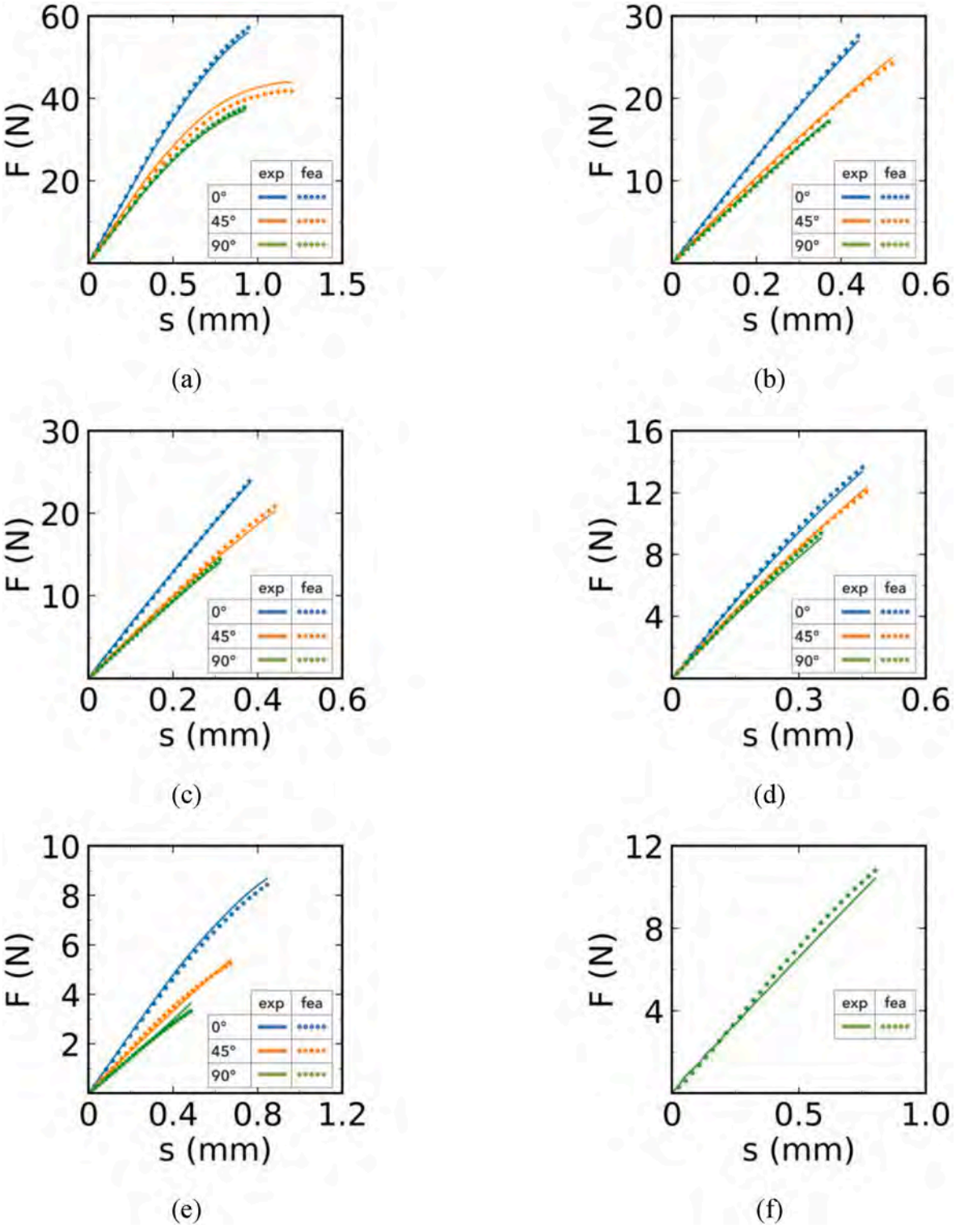

Fig. 8. Comparison of the Force (F) vs. displacement (s) behaviour for (a) dog bone, (b) dog bone with notch, (c) dog bone with hole, (d) shear, (e) Nakajima, and (f) disk specimens. Measurements were obtained from experiments (exp) and finite element analysis (FEA) using the coupled FE workflow (Ansys® Material Designer + Ansys® Mechanical). All force values are presented normalized by arbitrary reference values for confidential purposes.

$$\Delta\varepsilon^{pl}_{eq.vonMises} = \sqrt{\frac{2}{3}\left[\left(\Delta\varepsilon^{pl}_{xx}\right)^2+\left(\Delta\varepsilon^{pl}_{yy}\right)^2+\left(\Delta\varepsilon^{pl}_{zz}\right)^2\right]+\frac{4}{3}\left[\left(\Delta\varepsilon^{pl}_{yz}\right)^2+\left(\Delta\varepsilon^{pl}_{zx}\right)^2+\left(\Delta\varepsilon^{pl}_{xy}\right)^2\right]} \quad (16)$$

for isotropic materials, and:

$$\Delta\varepsilon^{pl}_{eq.Hill} = \sqrt{\frac{F\left(\Delta\varepsilon^{pl}_{11}\right)^2+G\left(\Delta\varepsilon^{pl}_{22}\right)^2+H\left(\Delta\varepsilon^{pl}_{33}\right)^2}{FG+FH+GH}+\frac{2\left(\Delta\varepsilon^{pl}_{23}\right)^2}{L}+\frac{2\left(\Delta\varepsilon^{pl}_{31}\right)^2}{M}+\frac{2\left(\Delta\varepsilon^{pl}_{12}\right)^2}{N}} \quad (17)$$

for anisotropic materials. The equivalent plastic strain, defined as the time integral of the equivalent plastic strain rate, simply becomes the sum over the simulation steps of the equivalent plastic strain increment as follows:

$$\varepsilon^{pl}_{eq} = \sum_{1}^{N}\Delta\varepsilon^{pl}_{eq,n} \quad (18)$$

Where N is the number of simulation steps, and $\Delta\varepsilon^{pl}_{eq,n}$ is the equivalent plastic strain increment computed for the *n-th* simulation step.

3. Results

3.1. Microstructure – fibre orientation analysis

Fig. 7(a) and b illustrate the fibre orientation tensor's diagonal components (a_{11}, a_{22}, a_{33}) and off-diagonal components (a_{12}, a_{23}, a_{13}) [35], respectively, plotted against the position across the specimen's thickness. These measurements were obtained from the analysis of μCT scans, specifically at the scanned position (centre of the plate). The coordinate system considered is depicted in Fig. 1(a), where the x-axis aligns with the flow direction, and the z-axis points in the thickness direction of the plate. In addition to the tensor-based orientation results, a representative μCT cross-section image is presented in Fig. 7(c) to visually illustrate the actual fibre structure within the scanned region. The image confirms the alignment trends seen in the tensor components: dominant in-plane alignment near the surfaces and more randomized or transverse orientation near the mid-plane. This qualitative visualization supports the quantitative orientation data extracted for the FE modelling.

3.2. Experimental vs. numerical

Fig. 8 depicts the force versus displacement curves of all the considered specimen configurations, both experimental and simulated. The force-displacement curves shown for each specimen type represent the average behaviour, calculated as the mean of the curves obtained from the individual tests conducted on each of the six specimens.

The measured and simulated forces have been normalized by an arbitrary value to maintain confidentiality. It is evident that the simulated curve closely matches the experimentally evaluated one, demonstrating a high level of accuracy. Values of the percent deviations between the area integrals (experiments vs. FEA) of all the cases reported in Fig. 8 are reported in Table 2.

For the dog bone specimens (in all orientations) and for the 0° Nakajima specimen, the force-displacement curves exhibit an initially linear response followed by a nonlinear response until failure. Conversely, a nearly linear response until failure was observed for all other specimens tested. Based on the results from the dog bone specimens, the material exhibits a ductile behaviour. However, a global (i.e. based on the force-displacement diagrams) quasi-brittle behaviour was observed in the notched specimens. This behaviour can be attributed to the stress concentration in the notch region, where the material experiences local plasticization.

Despite the globally linear behaviour observed in the force-displacement curves for most specimens, SEM analysis of the fracture surfaces revealed evidence of plastic deformation of the matrix at the micro-scale, as shown in the next section. This indicates that, while the overall macroscopic response appears predominantly elastic with limited plasticity, localized plastic deformation occurs in critical regions and stress concentration sites.

To validate the FE strain predictions and justify the selection of the triaxiality evaluation point, a comparison between experimental and numerical strain fields was performed. Fig. 9(a) shows the DIC-derived major strain field of a disk specimen at the last recorded frame before fracture, as an example, while Fig. 9(b) displays the corresponding FE strain field at the same applied load.

3.3. Fracture surface analysis

SEM analysis of the specimens' fracture surfaces revealed two separate zones: a smaller micro-ductile area marked by matrix deformation and a larger micro-brittle region indicative of brittle fracture behaviour. Similar fracture patterns in SFRPs have also been documented in previous studies [36–38].

To illustrate these areas in greater detail, the SEM images use color-coded contours to represent different levels of magnification:

- Blue Contour: Indicates regions selected for intermediate magnification, offering a closer examination of the fracture surface.

Table 2
Values of the percent deviations between the area integrals (experimental vs. fea).

		$\%\ \mathrm{Dev} = \left(\frac{fea-exp}{exp}\right)\times 100$		
Specimen	Plot index Fig. 8	0°	45°	90°
Dog bone	a	2.1	−4.7	2.0
Dog bone with notch	b	0.98	−1.76	−1.52
Dog bone with hole	c	−0.22	2.6	1.8
Shear	d	2.83	−0.33	4.2
Nakajima	e	−2.9	2.7	3.6
Disk	f	5.2		

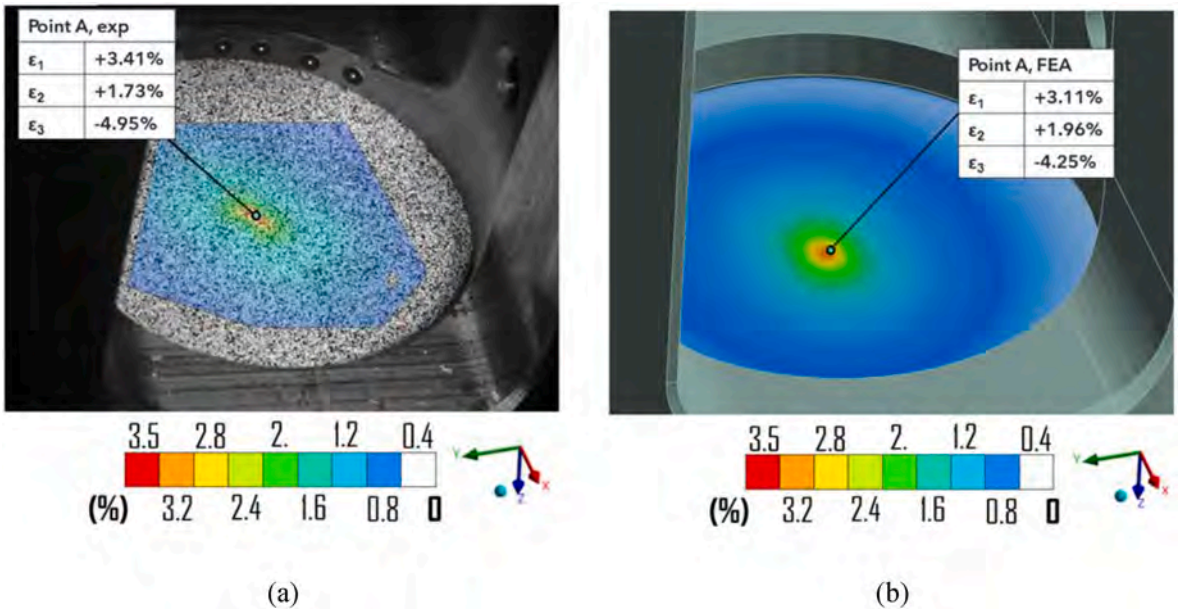

Fig. 9. (a) local principal strain values from DIC for the disk specimen; (b) local principal strain values evaluated using FEA for the disk specimen.
Point A, located at the centre of the specimen, corresponds to the area of maximum principal strain in both experimental and numerical data. The values of the three principal strains at this point ($\varepsilon 1$, $\varepsilon 2$, $\varepsilon 3$) are reported for both methods and demonstrate strong agreement. This confirms the fidelity of the simulation and supports the use of this node for triaxiality-based failure modelling.

- Red Contour: Highlights areas observed under high magnification, revealing intricate microstructural features such as fibre pull-out, matrix deformation, and fracture mechanisms.

Figs. 10–12 present SEM analyses of fracture surfaces for three different specimen types: a 90° dog bone with hole (Fig. 10), a 90° dog bone with notch (Fig. 11), and a 0° dog bone specimen (Fig. 12). Each figure follows a consistent structure, progressing from a CAD model and low-magnification overview to medium and high magnification images. The key microstructural features are annotated in subfigures (d) of each figure, where the highest magnification enables detailed visualisation of fracture mechanisms. These include (x) micro-ductile matrix deformation, (j) micro-brittle matrix fracture, (w) fibre fracture, and (z) fibre pull-out.

The micro-ductile zones (x) are characterised by plastic matrix deformation, while micro-brittle regions (j) exhibit angular fracture facets. Fibre breakage (w) and pull-out (z) are common features across all samples, although their prominence and spatial distribution vary depending on the specimen geometry and loading direction. The consistent identification of these mechanisms helps to link the micro-scale fracture behaviour with the macroscopic mechanical response observed during testing.

3.4. Evaluation of triaxiality and equivalent plastic strain using FEA

After successful validation of the FEA with respect to stiffness and local strain prediction, stress triaxiality could be reliably computed. The stress triaxiality and equivalent plastic strain values reported in this section were extracted from the numerical simulations at the nodes displayed in Fig. 4 The node selection was specimen-specific and performed by choosing nodes within the highly strained regions identified through both DIC measurements and finite element simulations for each configuration. This approach ensured alignment with the areas of maximum strain concentration prior to failure. For the dog bone specimens tested at 0°, 45°, and 90°, fracture consistently initiated in the same region of the gauge section, thereby reinforcing the validity and consistency of the node selection methodology for triaxiality extraction.

Failure strain was defined based on the last DIC frame prior to the first observable load drop or crack initiation, ensuring that damage accumulation was minimal and the simulation results were still representative of the undamaged or pre-critical state. The strain field and the applied force at this critical experimental frame were matched with the corresponding numerical simulation step. Consequently, triaxiality and equivalent plastic strain were extracted from the FE simulation at nodes corresponding to these experimentally observed failure locations.

Since the FE models employed did not incorporate progressive damage or element deletion, identifying the failure moment through experimental observations provided a consistent reference across different specimen geometries and orientations. The absence of explicit damage modelling is recognized as a limitation of the current approach.

3.4.1. Analysis based on stresses evaluated at the macro scale

According to Eq. (1), the evolution of triaxiality with the magnitude of plastic deformation was computed at composite level. Fig. 13 shows, for representative reasons, the evolution of triaxiality for the dog bone specimen across the three different orientations. For the sake of

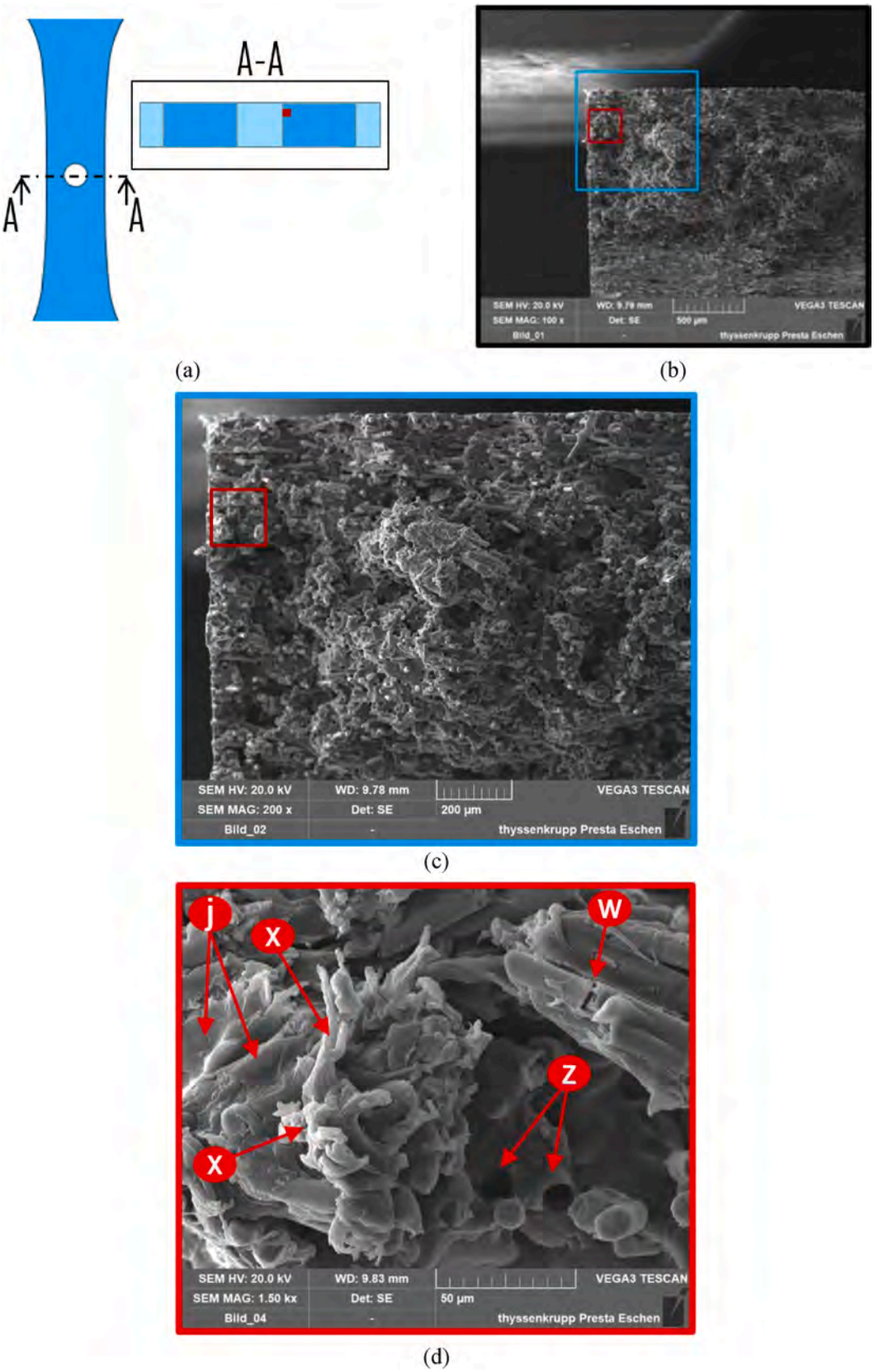

Fig. 10. (a) CAD model of the analysed 90° dog bone with hole specimen, indicating the locations where SEM analyses were performed. (b) SEM image showing an overview of the analysed areas. The red and blue squares indicate regions selected for higher-magnification SEM analyses shown in (c) and (d). (c) SEM image at medium magnification. (d) SEM image at maximum magnification, focusing on ductile regions and their microstructural characteristics. Annotated features highlight typical fracture mechanisms: (w) fibre fracture, (j) micro-brittle matrix fracture, (x) micro-ductile deformation of the matrix, and (z) fibre pull-out.

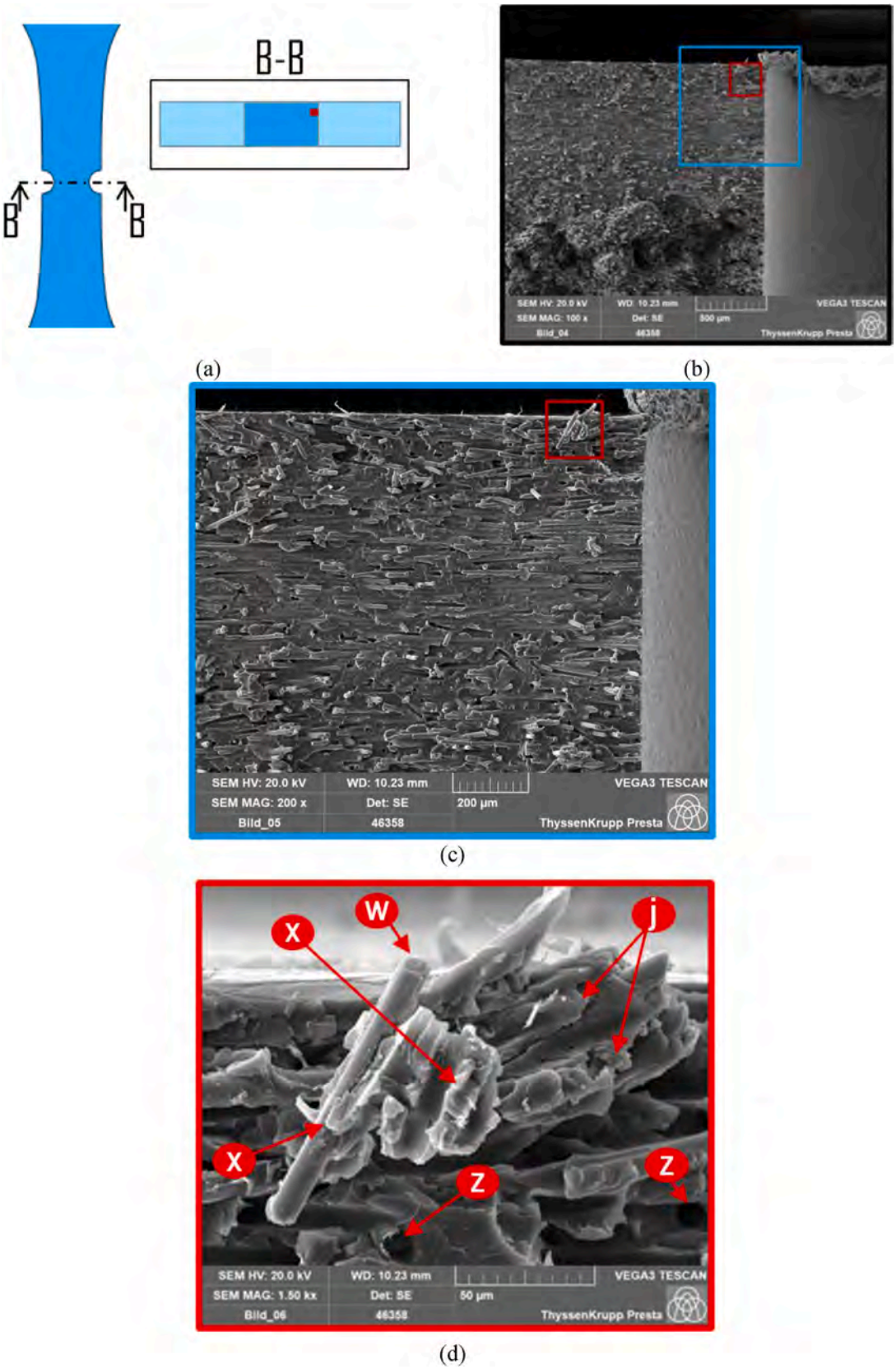

Fig. 11. (a) CAD model of the analysed 90° dog bone with notch specimen, indicating the locations where SEM analyses were performed. (b) SEM image showing an overview of the analysed areas. The red and blue squares indicate regions selected for higher-magnification SEM analyses shown in (c) and (d). (c) SEM image at medium magnification. (d) SEM image at maximum magnification, focusing on ductile regions and their microstructural characteristics. Annotated features highlight typical fracture mechanisms: (w) fibre fracture, (j) micro-brittle matrix fracture, (x) micro-ductile deformation of the matrix, and (z) fibre pull-out.

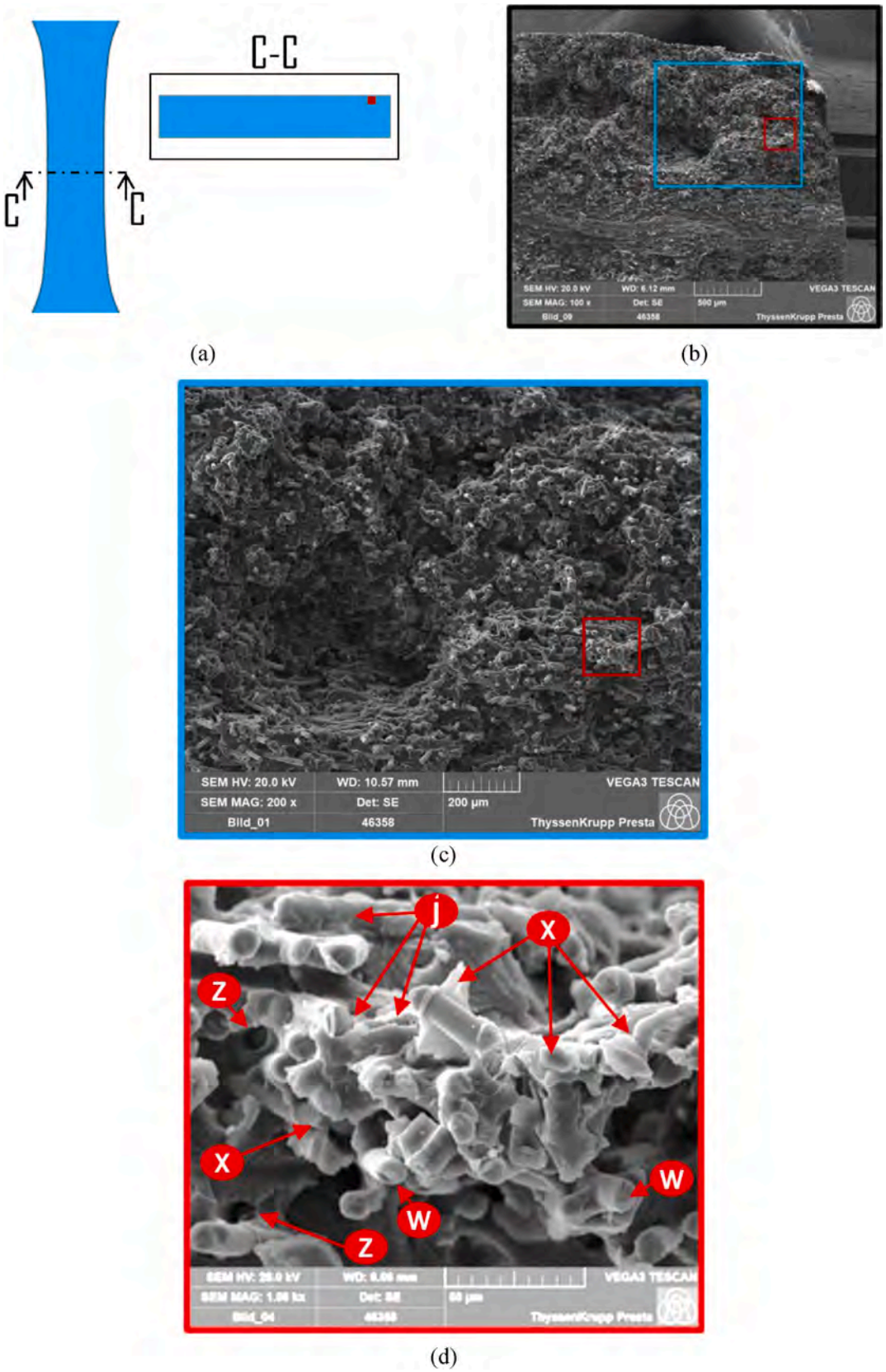

Fig. 12. (a) CAD model of the analysed 0° dog bone specimen, indicating the locations where SEM analyses were performed. (b) SEM image showing an overview of the analysed areas. The red and blue squares indicate regions selected for higher-magnification SEM analyses shown in (c) and (d). (c) SEM image at medium magnification. (d) SEM image at maximum magnification, focusing on ductile regions and their microstructural characteristics. Annotated features highlight typical fracture mechanisms: (w) fibre fracture, (j) micro-brittle matrix fracture, (x) micro-ductile deformation of the matrix, and (z) fibre pull-out.

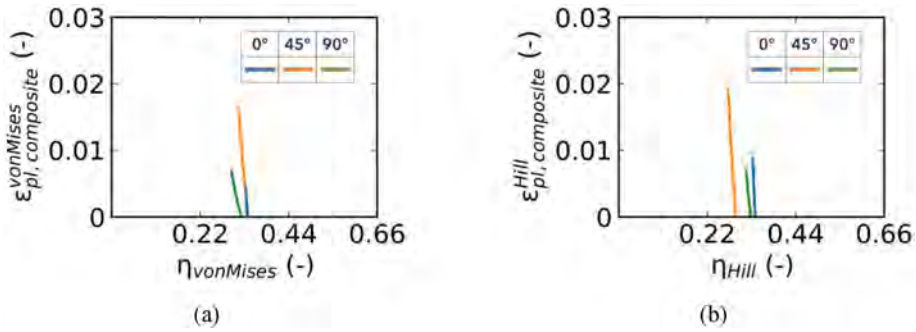

Fig. 13. (a) Von Mises and (b) Hill triaxiality vs. von Mises and Hill equivalent plastic strain on composite level for the dog bone specimen.

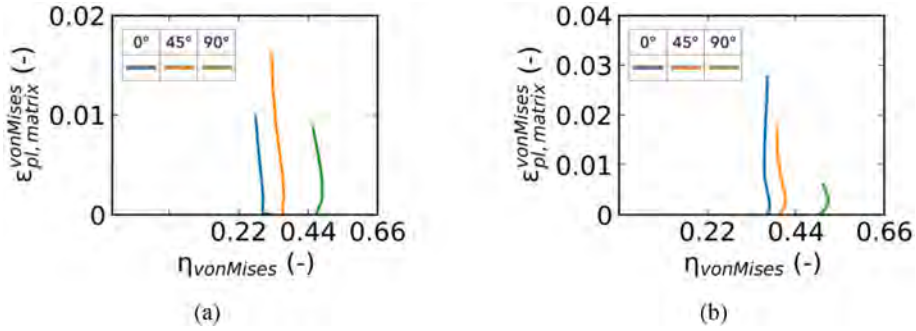

Fig. 14. Triaxiality vs. equivalent von Mises plastic strain at the matrix scale. Triaxiality calculated using the von Mises equivalent stress for the (a) dog bone and (b) Nakajima specimens.

Table 3
Triaxiality (−) and equivalent plastic strain (mm/mm) across specimen's orientations at failure.

		Composite (Macro-scale)				Matrix (Micro-scale)	
Specimen	Orientation (°)	$\eta_{VonMises}$	$\varepsilon_{pl}^{vonMises}$	η_{Hill}	ε_{pl}^{Hill}	$\eta_{VonMises}$	$\varepsilon_{pl}^{vonMises}$
Dog bone (db)	0	0.33	0.0044	0.33	0.0285	0.27	0.0098
	45	0.31	0.0163	0.27	0.0192	0.32	0.0161
	90	0.30	0.0068	0.32	0.0068	0.46	0.0087
Dog bone with notch (db + n)	0	0.43	0.0135	0.43	0.0166	0.35	0.0214
	45	0.45	0.0255	0.46	0.0316	0.37	0.0317
	90	0.40	0.0085	0.39	0.0110	0.47	0.0096
Dog bone with hole (db + h)	0	0.43	0.0133	0.43	0.0184	0.44	0.0173
	45	0.49	0.0246	0.50	0.0307	0.39	0.0294
	90	0.42	0.0073	0.42	0.0095	0.51	0.0086
Shear	0	0.08	0.0038	0.07	0.0048	0.10	0.0070
	45	0.03	0.0010	0.15	0.0012	0.28	0.0025
	90	0.10	0.0005	0.09	0.0394	0.11	0.0012
Nakajima	0	0.39	0.0249	0.41	0.0087	0.37	0.0277
	45	0.42	0.0158	0.36	0.0187	0.39	0.0175
	90	0.37	0.0053	0.36	0.0053	0.51	0.0061
Disk	–	0.61	0.0362	0.55	0.0394	0.62	0.0422

completeness all the other curves are reported in Appendix 1. Both isotropic and anisotropic approaches were employed, utilizing the von Mises and Hill equivalent stresses, along with the corresponding definition of the equivalent plastic strain for these calculations, respectively. It appears that regardless of the calculation method employed (von Mises or Hill), the stress triaxiality evolves uniquely and differently for each specimen and local fibre orientation with the amount of plastic strain.

The von Mises triaxiality values align closely with nominal values for isotropic materials at the onset of plasticity for both normal dog bone (0.33) and disk (0.66) specimens. However, deviations occur with increased plasticity, shifting towards shear-dominated regions for dog bone specimens and uniaxial regions for disk specimens. Similarly, Hill's triaxiality for normal dog bone specimens values align with nominal ones for uniaxial loading at onset of plasticity but vary with orientation and plasticity level. Shear specimens (Fig. A1c) at 0° and 90° show similar triaxiality values for both the yield models considered, while notable differences are observed for the 45° orientation. The Nakajima specimen (Fig. A1d) displays consistent von Mises's initial triaxiality across all the orientations which however varies with plasticity.

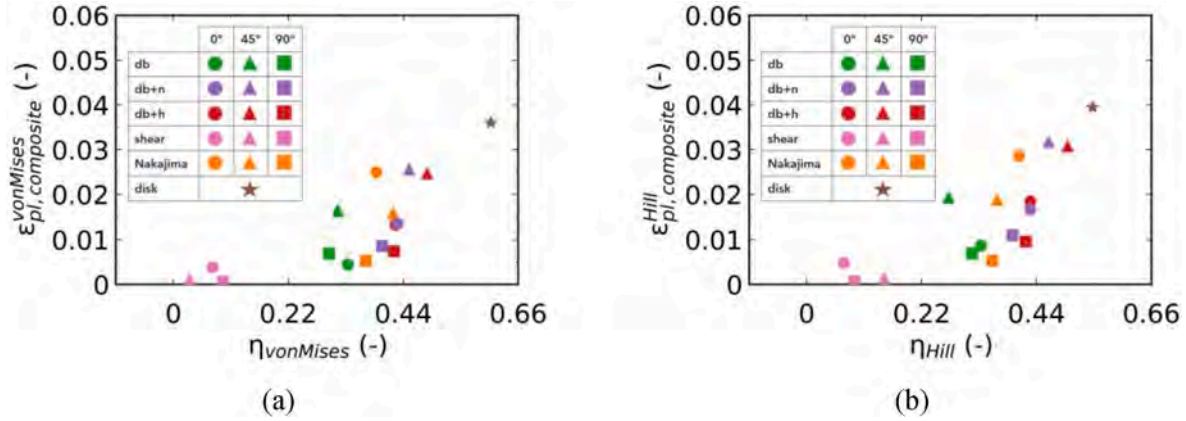

Fig. 15. (a) von Mises triaxiality vs. von Mises equivalent plastic strain and (b) Hill triaxiality vs. Hill equivalent plastic strain at the composite scale level for various specimens and orientations.

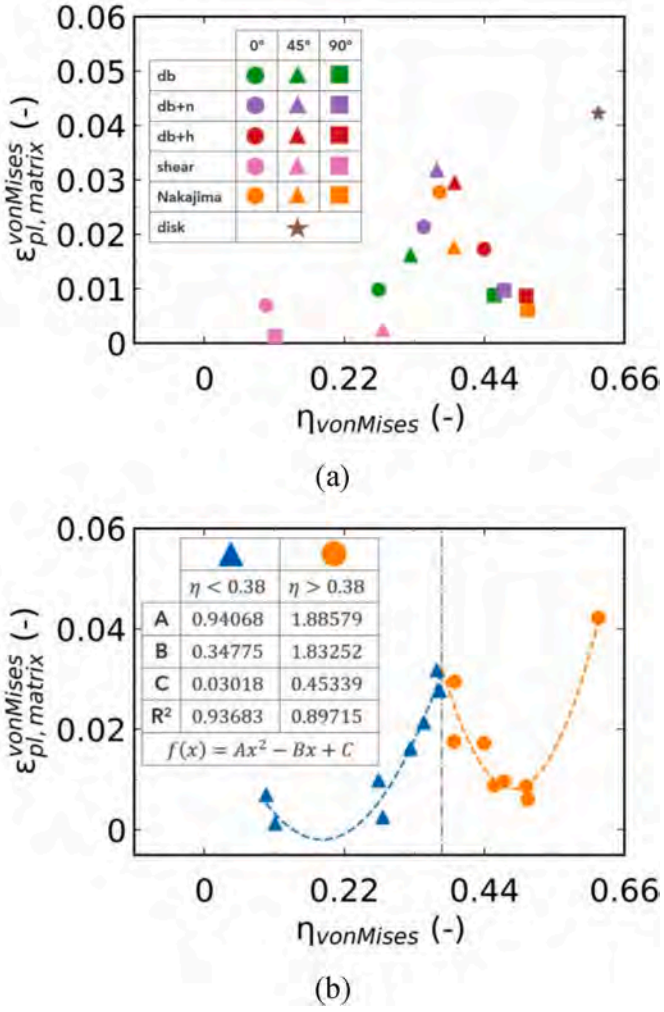

Fig. 16. (a) von Mises triaxiality vs. equivalent von Mises plastic strain evaluated on matrix scale level for different specimens and orientations. (b) von Mises triaxiality vs. equivalent plastic strain evaluated on matrix scale level including polynomian fitting curves.

The Hill's triaxiality of the Nakajima specimens (Fig. A1i) appreciably differ between orientations. Dog bone specimens with notches (Fig. A1a and f) and holes (Fig. A1b and g) exhibit similar evolution trends of triaxiality with plasticity, for both von Mises and Hill approaches. Overall, while von Mises and Hill's triaxiality generally align, discrepancies exist for specific specimens, especially those with remarkable anisotropic microstructures.

The equivalent plastic strain varies with the isotropic/anisotropic approach considered at the composite level. In general, for the same specimen, a higher equivalent plastic strain was observed for Hill compared to von Mises.

3.4.2. Analysis based on stresses evaluated at the micro-scale

Fig. 14 shows the results of the von Mises triaxiality and equivalent plastic strain computed at the matrix level. For representative purposes, only the evolution of the triaxiality of the dog bone and Nakajima specimens was presented. Further plots for all the specimens are available in Appendix 1. Distinct stress triaxiality values were observed across various specimen configurations and for different orientations of the same specimen geometry, indicating a strong dependence of the matrix behaviour upon the presence of the fibres and upon their orientation distribution.

Considering the 0° normal dog bone specimen, the predominant alignment of the fibres with the load maximizes the stress transfer occurring via fibre-matrix interfacial shear stresses. As a result, the stress state of the matrix likely consists of a combination of normal and shear stresses, leading to a stress triaxiality in the matrix slightly below the nominal 0.33 value for ideal uniaxial loading. Conversely, the normal 90° dog bone specimen likely experiences a constrained deformation of the matrix: the preferential transverse orientation of the fibres to the load hinders the Poisson's contraction of the longitudinally stretched matrix. This leads to stress amplification in the matrix and consequently to a deviation from ideal uniaxial stress state towards a plane strain condition under uniaxial loading. Intermediate orientation seemingly mitigates these effects, resulting in stress triaxiality of the 45° normal dog bone specimen (Fig. 14(a)) akin to the nominal 0.33 for uniaxial loading.

The disk specimen (Fig. A2d) initially retained nominal values of matrix triaxiality for an ideal biaxial loading, which slightly decreased with plasticity. The triaxiality in the matrix of shear specimens (Fig. A2c) aligns with nominal values of ideal shear for the 0° and 90° specimens, while it deviates for the 45° one. The matrix triaxiality of the 90° Nakajima specimen (Fig. 14(b)) showed conspicuous differences compared to that of its 0° and 45° counterparts, likely due to transverse fibre orientation hindering the matrix contraction. Dog bone specimens at 45° and 90°, with notches (Fig. A2a) and holes (Fig. A2b), displayed similar trends and values for the matrix level triaxiality. Remarkable difference is observed instead for the matrix level triaxiality of their 0° counterparts, despite a similar evolution with plasticity.

These findings underscore the complex interplay between specimen geometry, fibre orientation, and matrix behaviour, emphasizing the need for comprehensive characterization in composite materials analysis.

Table 3 presents the triaxiality and equivalent plastic strain values as discussed above, reflecting the diverse mechanical responses observed across different specimen orientations and loading conditions.

4. Triaxiality failure diagrams

The equivalent plastic strain values presented in this chapter are derived directly from the elasto-plastic material models implemented in the finite element (FE) analysis. These models were calibrated using experimental data and microstructural characteristics, ensuring their validity and relevance to the material under investigation (see Section 2.3.1). At the macroscopic level (e.g., force vs. displacement curves), plastic strain may appear negligible for some specimens. However, SEM analysis and numerical results demonstrate that, at a local level—particularly near critical regions such as notches—plasticity and equivalent plastic strain can be significant. This highly localized plastic behaviour plays a critical role in understanding failure initiation mechanisms.

It is also important to note that while equivalent plastic strain values at the composite and microstructural levels may show minor differences, the calculated triaxiality values vary significantly between the two approaches. This distinction is a key finding of our analysis and highlights the necessity of accurately capturing triaxiality, as it has a substantial impact on failure prediction and the evolution of plasticity under different loading scenarios.

4.1. Analyses at the macro-scale

In Fig. 15(a) and (b) the failure points were plotted in terms of composite level triaxiality vs. the equivalent plastic strain in the TFD for the Von Mises and Hill approach, respectively.

In the triaxiality investigation at the composite level using isotropic von Mises (as depicted in Fig. 15(a)), a clear correlation between stress triaxiality and von Mises equivalent plastic strain in the TFD could not be identified. None of the fitting methods proposed in literature for anisotropic material [19,23,39] suits the whole dataset, even if data sub-sets for specific fibre orientations or loading configurations are considered. Similarly, in the case of the Hill triaxiality (as observed in Fig. 15(b)), none of the methods proposed in the literature for fitting the data on the TFD are applicable to the present dataset. This is likely due to the high fibre volume content analysed in this work (50 %), as previous studies [23,39] considered a maximum fibre content of 20 %. It is therefore concluded that macro-scale approaches must be applied with caution when dealing with composites with higher volume fractions.

4.2. Analysis at the micro-scale

The TFD in Fig. 16(a) shows the triaxiality calculated using the Von Mises equivalent stress plotted against the equivalent plastic strain, at matrix level for each specimen investigated.

At the matrix level, as shown in Fig. 16(a), the shear specimens failed at the lowest plastic strain, indicating a stress triaxiality approaching zero, akin to the nominal triaxiality of an isotropic material subjected to perfect shear loading. In contrast, the disk specimen exhibited failure at the highest strain, with a stress triaxiality close to 0.66, resembling the nominal triaxiality of an isotropic material under a perfect biaxial stress state. Intermediate values of strains and triaxiality resulted in failure in the Nakajima, dog bone (plain, double notched, and with a hole) specimens.

Moreover, a clear division emerges at a triaxiality value of 0.38. This separation delineates two distinct groups within the scatter. As plotted in Fig. 16(b), the two emerging groups could be described using second-order polynomial fits, whose combination results in the failure curve, which describes the stress triaxiality dependent equivalent plastic strain limit values that the composite's matrix undergo without experiencing failure. The trend of the matrix failure curve aligns with those reported in referenced work for rolled aluminium and dual-phase steel sheet anisotropic materials [15,17,33,40,41]. However, the findings from the application of a similar methodology presented in this work to anisotropic metals [15,17,33,40,41] encompass different limit curves which retain the same trend while being shifted upward or downward

depending on the principal orientation of the microstructure to the load, as shown in Fig. 4(d) of Park [17] for specimen obtained from a metal sheet along three different orientations: parallel, diagonally and transversally to the rolling direction.

In the present investigation, by considering the composite-level anisotropy, stresses and strains, no clear relationships between the failure points could be found. Conversely, by considering the matrix-level isotropy, stresses and strains, the failure points collapsed into a single limit curve, thus becoming independent of the microstructure (fibres) orientations relative to the loading direction. It should be noted that the application of the Von-Mises yield criterion for the polymeric matrix, which assumes the material incompressibility at onset of yielding might be a limitation of the work. However, unlike metals, polymeric material could display a yielding behaviour which is sensitive to the applied hydrostatic stress (pressure), as reported by Jerabek [42]. Therefore, a pressure dependent yield function, as that concerned in the Drucker-Prager yield criterion [43], should be considered in future developments of the analysis.

Finally, it should be noted that the proposed microscale approach was developed for a composite with a high fibre volume fraction, thereby addressing the limitations of traditional macroscale approaches.

5. Conclusion

The present study extensively investigates the quasi-static behaviour of a PA6T/6I-GF50 composite through various experimental and numerical analyses. Test specimens of 3 mm thickness and various shapes were extracted from injection-moulded plates, with fibre orientations of 0°, 45°, and 90°. Micro-computed tomography scans provided a detailed evaluation of the microstructure of the injection-moulded plates. Stress triaxiality and equivalent plastic strain were computed both at the macro-scale, considering the composite as a whole, and at the micro-scale within the matrix using experimentally validated finite element (FE) simulations. Two yield models —von Mises (isotropic) and Hill 48 (anisotropic)—were employed to evaluate the material's macro-scale behaviour, as suggested in Ref. [23]. However, neither model successfully identified a clear failure trend in the triaxiality vs. equivalent plastic strain diagrams across all specimens.

To overcome the macro-scale limitations, it was thus proposed a micro-scale numerical approach, which distinguishes more clearly between the stresses in the matrix and in the fibres. This new triaxiality calculated in the matrix at the micro-scale according to the von Mises yield model revealed a distinct trend when plotted against the equivalent plastic strain in the matrix. These findings were further supported by SEM analysis of fracture surfaces, which showed localised plastic deformation in the matrix near critical regions.

This micro-scale trend forms the basis for defining a material-specific failure curve, similar to the FKM-NL guideline used in the automotive industry. Such a limit failure curve represents a characteristic material property that defines the failure threshold under specific loading conditions.

The identified matrix limit failure curve could be integrated into conventional FE tools as a valuable design aid for SFRP components. Rather than being used for direct failure predictions, this implementation combines experimental results and FE analysis to derive failure curves specific to the material's behaviour under various loading conditions. These curves aim to enabling engineers to optimise component designs, improving reliability and performance.

By incorporating these failure curves into FE tools, engineers can better assess failure risks in SFRP components and gain deeper insights into material behaviour beyond conventional uniaxial testing. This approach bridges the gap between experimental data and practical applications, enhancing the overall design process and supporting the development of more refined and robust predictive models for SFRPs. The proposed TFD-based approach offers a promising alternative to conventional uniaxial failure criteria, particularly for complex loading and geometries. Future research should include a direct comparison with standard failure models to further validate and potentially generalise the method.

CRediT authorship contribution statement

F.E. Fiorini: Writing – review & editing, Writing – original draft, Visualization, Validation, Project administration, Methodology, Investigation, Conceptualization. **A. Canegrati:** Writing – original draft, Visualization, Methodology, Conceptualization. **L.M. Martulli:** Writing – review & editing, Supervision, Conceptualization. **P. Steck:** Writing – review & editing, Supervision. **A. Bernasconi:** Writing – review & editing, Supervision, Conceptualization.

Declaration of competing interest

The authors declare that they have no known competing financial interests or personal relationships that could have appeared to influence the work reported in this paper.

Acknowledgements

The authors gratefully acknowledge thyssenkrupp Presta AG and BASF SE for supporting this work. The authors wish to thank Dr. Andreas Radtke (BASF SE) for assisting in moulding the plates and supporting this work, as well as Thorsten Wiege (maXerial AG) for performing the micro-CT scans. Finally, FEF gratefully acknowledges Sabina Hodžić (thyssenkrupp Presta AG) for her proofreading.

Appendix A. Supplementary data

Supplementary data to this article can be found online at https://doi.org/10.1016/j.polymertesting.2025.108927.

Appendix 1

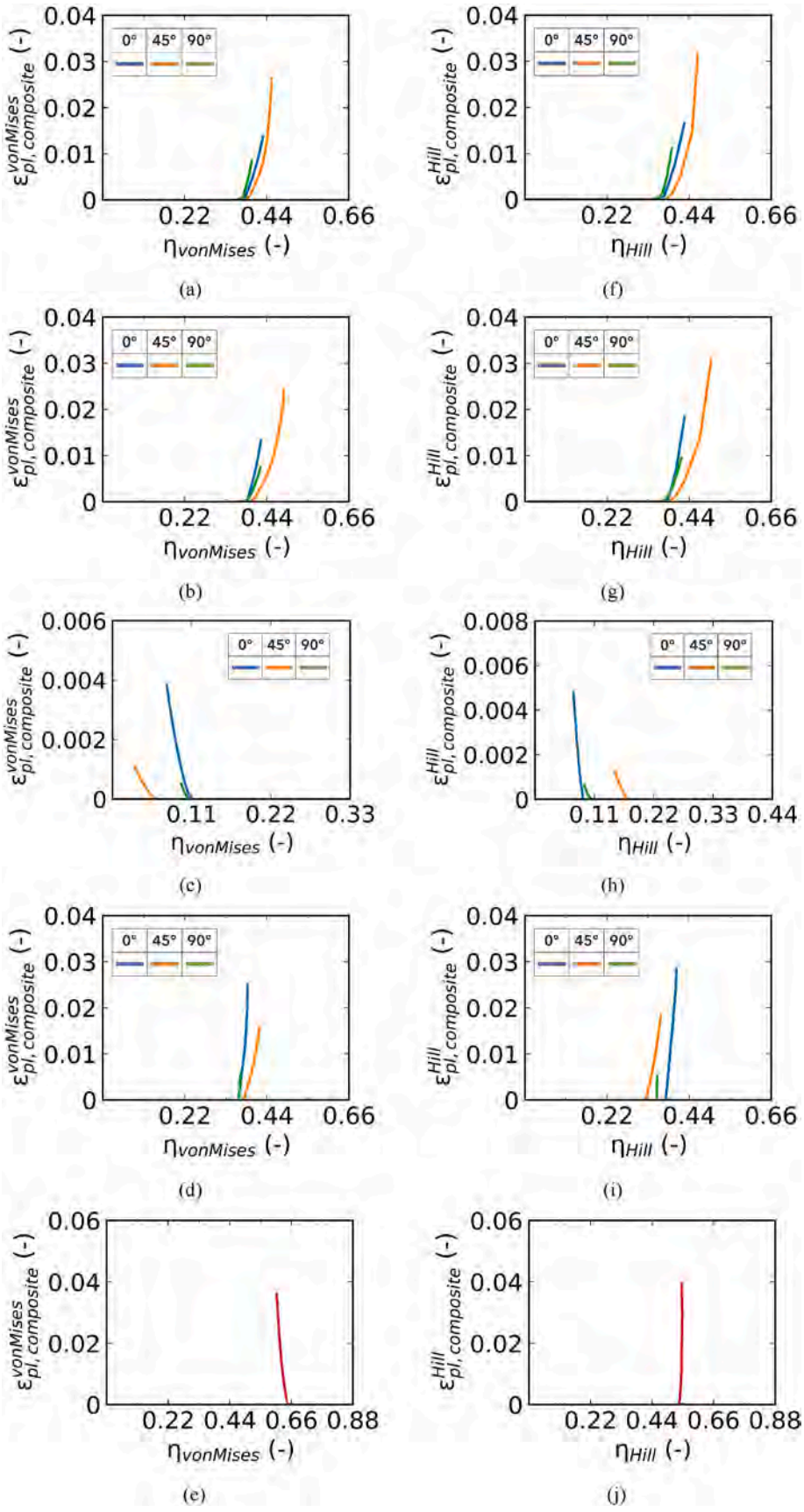

Fig. A.1. illustrates the relationship between triaxiality and equivalent plastic strain on the composite level, comparing von Mises and Hill criteria across various specimen geometries.

Figure A.1(a-e)Von Mises and (f-j) Hill triaxiality vs. von Mises and Hill equivalent plastic strain on composite level for (a, f) dog bone with notch, (b, g) dog bone with hole, (c, h) shear, (d, i) Nakajima, and (e, j) disk specimens.

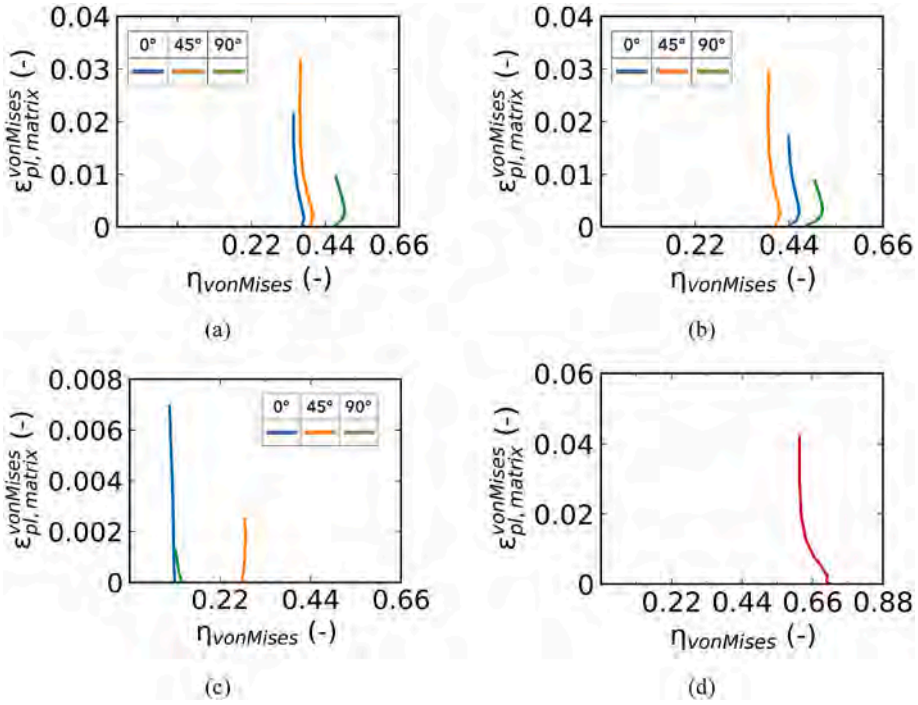

Fig. A.2. presents the triaxiality versus equivalent von Mises plastic strain at the matrix scale, calculated using the von Mises equivalent stress for various specimen geometries.

Figure A.2(a-d) Triaxiality vs. equivalent von Mises plastic strain at the matrix scale. Triaxiality calculated using the von Mises equivalent stress for (a) dog bone with notch, (b) dog bone with hole, (c) shear, and (d) disk specimens.

Data availability

The data that has been used is confidential.

References

[1] A. Bernasconi, P. Davoli, A. Basile, A. Filippi, Effect of fibre orientation on the fatigue behaviour of a short glass fibre reinforced polyamide-6, Int. J. Fatig. 29 (2007) 199–208.

[2] W.K. Chin, H.T. Liu, Y.D. Lee, Effects of fiber length and orientation distribution on the elastic modulus of short fiber reinforced thermoplastics, Polym. Compos. 9 (1988) 27–35.

[3] S.-Y. Fu, B. Lauke, Effects of fiber length and fiber orientation distributions on the tensile strength of short-fiber-reinforced polymers, Compos. Sci. Technol. 56 (1996) 1179–1190.

[4] A. Bernasconi, F. Cosmi, D. Dreossi, Local anisotropy analysis of injection moulded fibre reinforced polymer composites, Compos. Sci. Technol. 68 (2008) 2574–2581.

[5] F.E. Fiorini, L.M. Martulli, P. Steck, A. Bernasconi, A modified energy-based fatigue parameter for short fiber reinforced polymers: performance analysis with varying thicknesses, load ratios, and fiber orientations, Fatigue Fract Eng M 46 (9) (2023) 3372–3386.

[6] K. Friedrich, Microstructural efficiency and fracture toughness of short fiber/thermoplastic matrix composites, Compos. Sci. Technol. 22 (1985) 43–74.

[7] M. Gupta, K. Wang, Fiber orientation and mechanical properties of short-fiber-reinforced injection-molded composites: simulated and experimental results, Polym. Compos. 14 (1993) 367–382.

[8] H. Xu, M. Kuczynska, N. Schafet, F. Welschinger, J. Hohe, FE-based damage modeling approach for short fiber reinforced thermoplastics under quasi-static load coupling anisotropic viscoplasticity and matrix degradation, J. Compos. Mater. 56 (2022) 3113–3125.

[9] T. Mori, K. Tanaka, Average stress in matrix and average elastic energy of materials with misfitting inclusions, Acta Metall. 21 (1973) 571–574.

[10] J.D. Eshelby, The determination of the elastic field of an ellipsoidal inclusion, and related problems, Proc. Roy. Soc. Lond. Math. Phys. Sci. 241 (1957) 376–396.

[11] I. Doghri, L. Tinel, Micromechanical modeling and computation of elasto-plastic materials reinforced with distributed-orientation fibers, Int. J. Plast. 21 (2005) 1919–1940.

[12] S. Kammoun, I. Doghri, L. Adam, G. Robert, L. Delannay, First pseudo-grain failure model for inelastic composites with misaligned short fibers, Compos Part Appl Sci Manuf 42 (2011) 1892–1902.

[13] B. Klimkeit, Y. Nadot, S. Castagnet, C. Nadot-Martin, C. Dumas, S. Bergamo, C. Sonsino, A. Büter, Multiaxial fatigue life assessment for reinforced polymers, Int. J. Fatig. 33 (2011) 766–780.

[14] S.W. Tsai, E.M. Wu, A general theory of strength for anisotropic materials, J. Compos. Mater. 5 (1971) 58–80.

[15] Y. Bao, T. Wierzbicki, On fracture locus in the equivalent strain and stress triaxiality space, Int. J. Mech. Sci. 46 (2004) 81–98.

[16] J. Peng, Y. Wang, Q. Dai, X. Liu, L. Liu, Z. Zhang, Effect of stress triaxiality on plastic damage evolution and failure mode for 316L notched specimen, Metals 9 (2019) 1067.

[17] N. Park, H. Huh, S.J. Lim, Y. Lou, Y.S. Kang, M.H. Seo, Fracture-based forming limit criteria for anisotropic materials in sheet metal forming, Int. J. Plast. 96 (2017) 1–35.

[18] R. Hill, A theory of the yielding and plastic flow of anisotropic metals, Proc. Roy. Soc. Lond. Math. Phys. Sci. 193 (1948) 281–297.

[19] F. Rickhey, S. Hong, Stress triaxiality in anisotropic metal sheets—Definition and experimental acquisition for numerical damage prediction, Materials 15 (2022) 3738.

[20] F. Barlat, K. Lian, Plastic behavior and stretchability of sheet metals. Part I: a yield function for orthotropic sheets under plane stress conditions, Int. J. Plast. 5 (1989) 51–66.

[21] P. Camanho, M. Bessa, G. Catalanotti, M. Vogler, R. Rolfes, Modeling the inelastic deformation and fracture of polymer composites–Part II: smeared crack model, Mech. Mater. 59 (2013) 36–49.

[22] M. Vogler, R. Rolfes, P. Camanho, Modeling the inelastic deformation and fracture of polymer composites–part I: plasticity model, Mech. Mater. 59 (2013) 50–64.

[23] L. Quagliato, J. Lee, J.H. Fonseca, D. Han, H. Lee, N. Kim, Influences of stress triaxiality and local fiber orientation on the failure strain for injection-molded carbon fiber reinforced polyamide-6, Eng. Fract. Mech. 250 (2021) 107784.

[24] F.i.V. Fkm, Analytical Strength Assessment 7th, 2020, 2020.

[25] Basf SE, Ultramid® Advanced T1000 (PA, PPA).

[26] ISO, Metallic Materials — Determination of forming-limit Curves for Sheet and strips-part 2: Determination of forming-limit Curves in the Laboratory, ISO, 2021.

[27] Waygate Technologies, Phoenix Micro CT Scanner.

[28] Volume Graphics, VGSTUDIO MAX.

[29] a.s. Tescan Group, TESCAN Vega-III high-resolution SEM.

[30] ARAMIS 3D Camera System.

[31] Ansys® Workbench 2022 R2.

[32] Ansys® Workbench 2022 R2, User Manual.

[33] D.-Z. Sun, Charakterisierung Und Modellierung Des Anisotropen Versagensverhaltens Von Aluminiumwerkstoffen Fuer Die Crashsimulation, FAT-Schriftenreihe, 2018.

[34] R.B. Colby, Equivalent Plastic Strain for the Hill's Yield Criterion Under General three-dimensional Loading, Massachusetts Institute of Technology, 2013.
[35] S.G. Advani, C.L. Tucker III, The use of tensors to describe and predict fiber orientation in short fiber composites, J. Rheol. 31 (1987) 751–784.
[36] M. De Monte, U.d.s.d. Firenze, A.m.s.U.d. Bologna, U.d.s.d. Padova, Multiaxial Fatigue Behaviour of Short Fibre Reinforced Thermoplastics: Tesi Di Dottorato, 2008.
[37] J. Horst, J. Spoormaker, Fatigue fracture mechanisms and fractography of short-glassfibre-reinforced polyamide 6, J. Mater. Sci. 32 (1997) 3641–3651.
[38] R. Lang, J. Manson, R. Hertzberg, Mechanisms of fatigue fracture in short glass fibre-reinforced polymers, J. Mater. Sci. 22 (1987) 4015–4030.
[39] R. Krivachy, Charakterisierung Und Modellierung Kurzfaserverstärkter Thermoplastischer Kunststoffe Zur Numerischen Simulation Von Crashvorgängen, Fraunhofer IRB Verlag, 2007.
[40] Z.A. Mehari, J. Han, Numerical prediction of ductile fracture during the partial heating roll forming process of DP980, Int. J. Fract. 234 (2022) 97–112.
[41] L. Qian, X. Wang, C. Sun, A. Dai, Correlation of macroscopic fracture behavior with microscopic fracture mechanism for AHSS sheet, Materials 12 (2019) 900.
[42] M. Jerabek, D. Tscharnuter, Z. Major, K. Ravi-Chandar, R. Lang, Multiaxial yield behaviour of polypropylene. EPJ Web of Conferences, EDP Sciences, 2010 03005.
[43] D. Drucker, W. Prager, Q. Appl Math, Soil Mechanics and Plastic Analysis or Limit Designs, vol. 10, 1952, pp. 157–165.